SPECTROSCOPIC STUDIES OF DEFECTS IN IONIC AND SEMI-IONIC SOLIDS

Johann-Martin Spaeth

University of Paderborn
Fachbereich Physik
Warburger Str. 100A, 4790 Paderborn, FRG

1. INTRODUCTION

The investigation of point defects in solids is of increasing importance for that part of solid state physics which often is referred to as 'materials science'. A small concentration of impurities or native defects can dominate many important bulk properties like electrical conductivity and optical and mechanical properties. For the development of materials for specific applications it is decisive to understand the defect structure. In 'simple' hosts like the alkali halides, the properties of 'model' defects like the F centre or atomic hydrogen on various sites have been studied in great detail and are rather well understood. The experimental tools were mostly spectroscopic techniques, which were to a great deal developed alongside with these studies. Currently the interest has focussed more on the application of these techniques to more complicated systems like hosts of a more complicated atomic structure, of semi-ionic or covalent nature and more complicated defects, be it due to the nature of the impurity, aggregation of impurities or of impurities and intrinsic defects, low symmetry etc.

In the last decade spectroscopy has greatly profited from the advancement of experimental techniques, especially from the use of microcomputers in experiments. Now the investigation of complicated systems, which are of practical importance,can be attempted. Examples are III-V semiconductor materials for microelectronics, the development of laser-active material (color centre lasers), radiation damage in material withstanding high temperatures.

In the series of 3 lectures it will not be possible to cover all current important spectroscopic techniques. Methods of defect identification, that is the determination of the 'atomic' and electronic structure, will be discussed predominantly, as well as the direct correlation of optical and structural defect properties. The most powerful method is the magnetic resonance spectroscopy, especially when applying the technique of multiple resonances, like electron nuclear double resonance (ENDOR), optically detected electron spin resonance (ODESR) and optically detected ENDOR (ODENDOR). The aim of the lectures is to introduce to these methods and to demonstrate their actual use. The examples given are mostly taken from the work of the Paderborn group as a matter of convenience.

2. OPTICAL ABSORPTION AND EMISSION

In ionic and semi-ionic crystals many defects have localised energy states within the band gap and possess optical absorptions with energies below the band gap energy. Fig. 1 shows this schematically for the transition from the defect ground state to the first excited state. The absorption is then observed within the 'optical window' of the crystal, where no band-band transitions ($h\omega > E_g$) and no transitions due to lattice vibrations occur. In the alkali halides this window ranges from about 6-10 eV to about 0.1 eV.

The correlation of such a defect-induced optical absorption with a particular defect is usually a difficult task. This is demonstrated, e.g. by the long history of the research on color centres in alkali halides (1). Assignments are mostly attempted by variation of the impurity concentration or the irradiation time, if it is an intrinsic defect like a vacancy, electron or hole centre as consequence of radiation damage. However, this is not always unambiguous. Several defects can be produced simultaneously with overlapping absorption bands. Often there is one characteristic lumincescence band. The measurement of its excitation spectrum can be used to identify the associated absorption bands provided no other defect luminescence bands overlap it strongly.

In ionic and semi-ionic crystals most defect states are sensitive to the positions of the nearby atoms or ions, so that the form of the absorption and the form and the energy position of the emission depend on the vibrations of the surrounding ions. This is conveniently discussed in the approximation of the configuration coordinate diagram (CC-diagram), in which the lattice vibrations are represented by a single localised mode with a configuration coordinate Q and linear coupling is assumed for the vibrational energy, resulting in a parabolic energy curve for both the ground and excited states (see Fig. 2). They have the form

$$E = 1/2\ KQ^2 \qquad 2.1$$

where K is a force constant. Absorption and emission are vertical transitions (Born-Oppenheimer approximation). After the electrical dipole transition of the absorption has occurred, the electron distribution is changed and accordingly the lattice will relax and adjust to a new equilibrium position represented by $Q_o + \Delta Q$ in Fig. 2. From the vibrational ground state of the excited state parabola the emission takes place into a ground state configuration, which has to relax back into the original configuration. The relaxation process involves phonon emission which is

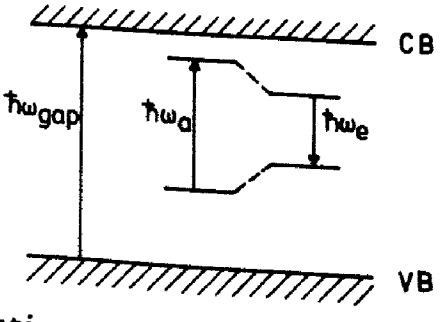

Fig. 1. Schematic representation of optical intracenter absorption and emission.

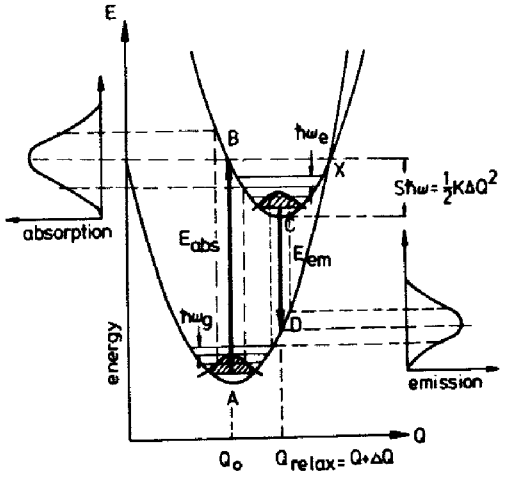

Fig. 2. CC-diagram of optical absorption and emission.

the reason for the observed Stokes shift ΔE between the energies of absorption and emission ($\Delta E = E_{abs} - E_{em}$). ΔQ is directly related to the strength of the electron phonon coupling, which is characterised by the Huang-Rhys factor S

$$S \cdot \hbar\omega = 1/2\ K \cdot \Delta Q^2 \qquad 2.2$$

where ω is the vibrational frequency (assumed to be equal in ground and excited states in the simplest approximation).

For large electron phonon coupling (S >10) the shapes of the absorption and emission bands are approximately Gaussian with a half-width proportional to $\hbar\omega \cdot \sqrt{S}$. This is indicated in Fig. 2. Typical half-widths are several tenths of an eV. As an example the lowest energy absorption of laser-active $F_A(Tl^+)$ centres and their emission bands in several alkali halides are shown in Fig. 3 (2). A discussion of the structure of these centres and their optical properties will be presented in sec.7.

If the coupling is weak (S < 1) both ground and excited state parabolae are hardly displaced against each other and the dominant feature is the 'zero phonon line' (ZPL). The transition involves no vibrational energies. Typical examples are transitions within the $4f^n$ configuration in rare earth ions in solids. The 4f configuration is well shielded (3).

In intermediate coupling (1<S<6) the ZPL is resolved, but the multiphonon structure is the dominant feature of the spectrum. The intensity of the ZPL relative to the whole band is given by exp (-S). It becomes undetectible for high values of S. An example for the absorption of a ZPL and a phonon replica structure is given in Fig. 4 for F_3-centres in LiF (4). For further details and the influence of the Jahn-Teller effect on the shape of the bands see (5,6).

When a ZPL can be measured, the application of uniaxial stress and magnetic and electrical fields can cause a splitting of the ZPL, from which structural information such as defect symmetry can be derived. (see e.g. Ref. 1, chapters 5 and 6 and further references therein).

Defects having a strong electron phonon coupling may not show a luminescence or only a very weak one. In the simple framework of the CC-diagram a nonradiative de-excitation occurs, when the excited state energy reached in a Frank-Condon absorption transition (point B in Fig. 2) lies

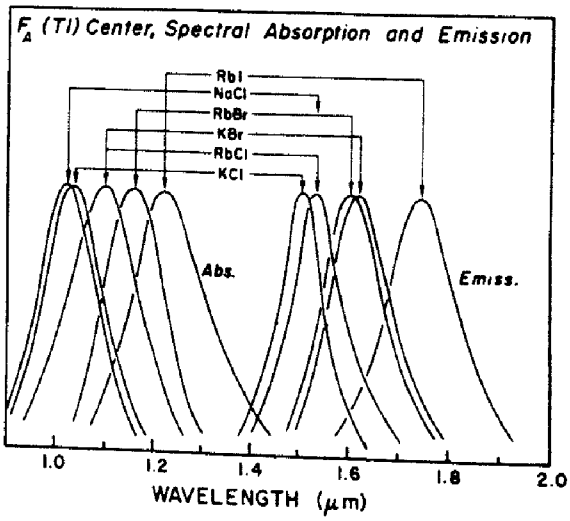

Fig. 3. Lowest energy absorption and emission of $F_A(Tl^+)$ centres in several alkali halides (After (2)).

above the intersection of ground and excited state potential energy curves (point C in Fig. 2). In this case the system can be de-excited through the intersection directly into the ground state under phonon emission. In the approximation of linear coupling and equal vibration frequencies for ground and excited state this occurs when $E_{em} < 1/2\ E_{abs}$ (Dexter-Klick-Russell-rule) (7,8).

3. ELECTRON SPIN RESONANCE (ESR)

Paramagnetic defects can be identified by means of electron spin resonance (ESR). Defect identification is based on the resolution of the hyperfine (hf) interactions, that is the interaction between the magnetic moment of the unpaired electron (or hole) and the magnetic moment of a central (impurity) nucleus or the magnetic moments of the nuclei of the surrounding lattice atoms. The latter interaction is mostly called ligand hyperfine or superhyperfine (shf) interaction. In ionic crystals ESR is, of course, restricted to defects which are paramagnetic in their ground state or which can be excited into paramagnetic excited states as in the case of many electron systems ($S > 1/2$). In semiconductors, there is often the possibility to 'make' the defects paramagnetic by raising or lowering the Fermi energy E_F. This can be achieved by additional doping of shallow donors or acceptors and is currently applied to the study of so-called deep level defects, which have levels near the middle of the band gap.

Fig. 5a shows schematically the basic ESR experiment. A magnetic dipole transition is induced between the Zeeman levels for $m_s = \pm 1/2$ if the resonance condition

$$\hbar\omega = g\beta_e B_o \qquad 3.1$$

is fulfilled. g is the electronic g-factor, β_e the Bohr magneton. Usually one varies the magnetic field and keeps ω constant (Fig. 5b). For fields around 0.3 T one uses microwave irradiation of $\sim$ 10 GHz (X-band) and for fields around 0.8 T radiation of $\sim$24 GHz (K-band). Upon resonance the microwave absorption is measured. (In order to be able to use lock-in techniques for sensitivity enhancement one measures the derivative of the absorption as consequence of magnetic field modulation) (9).

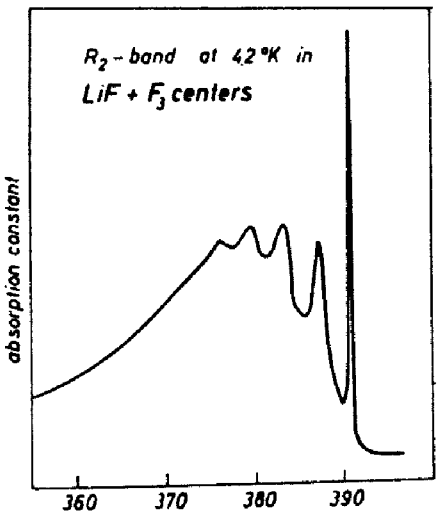

Fig. 4. Absorption spectrum of the R_2-band of F_3-centres in LiF. After (4).

The experiment of Fig. 5 does not give much information on the defect structure although deviations of the g-factor from the value of the free electron (g_e = 2.0023) contain some relevant information (9,10). Defect identification is based on the splitting of such a resonance line due to hf or shf interactions. Fig. 6 shows the level diagram for the simple case of the hf splitting due to a nucleus with I = 1/2. According to the ESR selection rules (9)

$$\Delta m_s = \pm 1, \quad \Delta m_I = 0 \qquad 3.2$$

there are now two ESR transitions split by the hf interaction constant A(θ). The resonances are described by the Spin Hamiltonian

$$\hat{H} = g\beta_e \vec{B}_o \hat{\vec{S}} + \hat{\vec{I}} \tilde{A} \hat{\vec{S}} - g_I \beta_n \vec{B}_o \hat{\vec{I}} \qquad 3.3$$

where β_n is the nuclear magneton, g_I the nuclear g-factor and $\tilde{A}$ the hf tensor. In perturbation theory of first order one obtains for the

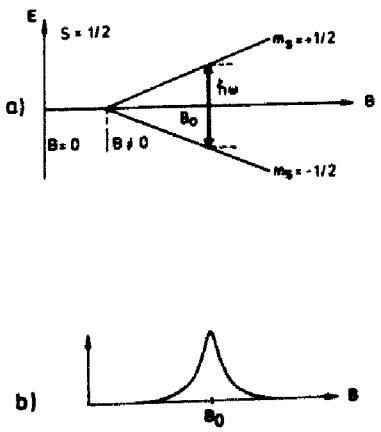

Fig. 5. Schematic representation of the basic ESR experiment.

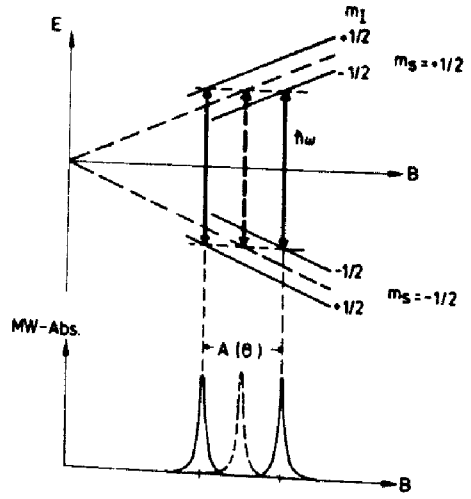

Fig. 6. Level diagram and ESR for a hyperfine interaction with a nucleus of I = 1/2.

resonance field positions

$$h\nu_{ESR} = g\beta_e B_{res} + m_I\, A(\theta) \qquad 3.4$$

Since the nuclear spin quantum number m_I has the two values $m_I = \pm 1/2$ and ν_{ESR} = constant, there are two resonance fields B_{res1} and B_{res2} separated by $A(\theta)/g\beta_e$.

Fig. 7 shows how a hf interaction can be used for defect identification for the example of Te^+ defects in Si (11). 92% of the Te isotopes are diamagnetic and give rise to the central ESR line near 3500 G (measured in X-band) corresponding to g ≈ 2. The two magnetic isotopes ^{125}Te (7% abundant) and ^{123}Te (0.9% abundant) both have I = 1/2 and according to (3.4) doublet splitting. The ESR line intensities follow the isotope abundance and the relative splittings are in the ratio of the respective nuclear moments (see below). Therefore the defect is unambiguously identified as being due to Te impurities. However, no further structure due to shf interactions is resolved. Therefore, the site of Te^+ in the lattice cannot be determined from ESR. Te^+ has an isotropic hf interaction. In general, the hf interaction is anisotropic and the spectrum is angular dependent as indicated in 3.4. Again, in first order and for axial symmetry of the defect the resonance fields are given by

$$h\nu_{ESR} = g\beta_e B_{res} + m_I\, (a + b\, (3\cos^2\theta - 1)) \qquad 3.5$$

where a is the isotropic hf constant, b the anisotropic hf constant. θ is the angle between the magnetic field B_o and the principal axis z of the hf tensor. In general, the interaction constants a and b and b' are related to the principal values of the hf tensor by

$$A = (a \cdot \underline{\tilde{I}} + \tilde{B}) \qquad 3.6$$

$$b = \frac{1}{2} B_{zz} \qquad 3.7$$

$$b' = \frac{1}{2} (B_{xx} - B_{yy}) \qquad 3.8$$

where b' describes the deviation from axial symmetry.

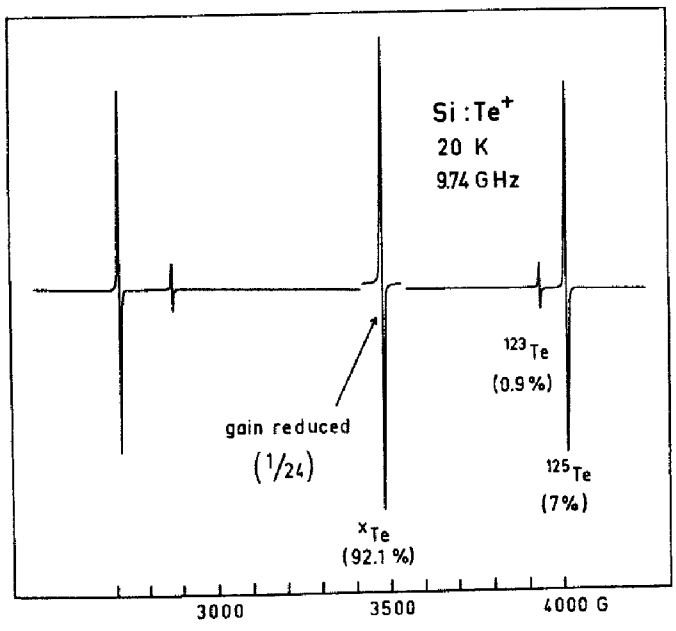

Fig. 7. ESR spectrum of Te^+ centres in Silicon. After (11).

Fig. 8a shows the ESR lines of $Tl^0(1)$ centres in KCl (and some other simultaneously produced defects). Again, since both Tl isotopes ^{203}Tl and ^{205}Tl have I = 1/2, the spectra consist of doublets. The splitting is, however, angular dependent. The angular dependence in Fig. 8b for rotation of the magnetic field in a (100)-plane shows this as well as the distribution of the centres in the crystal with respect to their axes. They have axial symmetry about a (100) direction. $Tl^0(1)$ centres are Tl^0 atoms next to an anion vacancy, while $Tl^0(2)$ centres have two anion vacancies next the atom (12). The angular dependence and isotope distribution leads here already to a structural model. ESR cannot reveal, however, whether Tl^0 resides precisely on a cation lattice site or is relaxed towards the vacancy, and it cannot either be said whether the vacancy is filled with another impurity since the angular dependence reflects only the tetragonal symmetry of the defect and not further shf structure is resolved.

Fig. 8a shows also another feature of conventional ESR spectroscopy. Since the ionising radiation producing these centres creates many defects simultaneously, it is not easy to unambiguously assign all the ESR lines to particular centres and follow their angular dependence. It will be shown below that with optical detection of the ESR each defect can be measured selectively, which greatly facilitates the analysis.

Fig. 9 shows the ESR spectrum of atomic hydrogen on interstitial sites, cation and anion vacancy sites in KCl (13). The central hf splitting with the proton (I = 1/2) is in all three cases practically the same. Only for the interstitial site a shf interaction with nearest neighbours (13) is resolved. The substitutional sites cannot be inferred from the ESR spectrum. They could be established only by resolving the shf interactions with ENDOR experiments.

The hf interaction constants are determined by the electronic wave function of the defects and the nuclear moments of the nuclei. In a simple one particle approximation the isotropic constant a is given by

$$a_1 = \frac{2\mu_0}{3} g\beta_e \, g_I \, \beta_n \, |\psi(r_1)|^2 \qquad 3.9$$

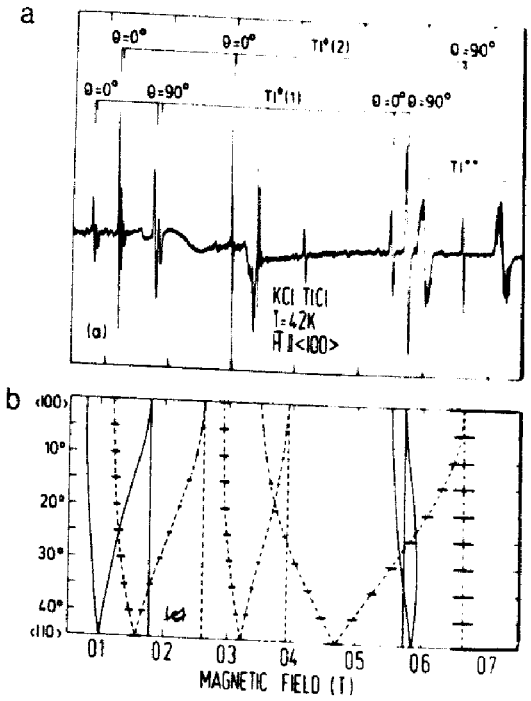

Fig. 8. (a) ESR spectrum of $Tl^{o}(1)$ and $Tl^{o}(2)$ centres in KCl:Tl for $B_o \| [100]$ measured at 42 K. After (12).
(b) The calculated angular variation of the spectra in a (100) plane. Straight lines are due to $Tl^{o}(1)$, broken lines are due to $Tl^{o}(2)$ centres. The horizontal bars indicate the transition probabilities for $Tl^{o}(2)$. After (12).

where $\psi(r)$ is the wave function of the defect, $\psi(r_1)$ its amplitude at the site r_1 of a particular nucleus. The anisotropic tensor elements are given by

$$B_{ik} = \frac{\mu_o}{4\pi} g\beta_e g_I \beta_n \int \left(\frac{3}{r^5} x_i x_k - \frac{1}{r^3} \delta_{ik}\right) |\psi(\vec{r})|^2 \, dV \qquad 3.10$$

$\vec{r}$ means the radius vector from the nuclear site of concern (origin) where the origin is spared in the integral of equ. (3.10) (10).

Thus the hf constants are proportional to g_I and therefore the interaction constants of different isotopes must be in the ratio of their respective g_I factors. This is used for their identification.

4. ELECTRON NUCLEAR DOUBLE RESONANCE (ENDOR)

The information needed for determining the defect structure is in its shf structure. The most direct way to measure it would be by measuring the nuclear magnetic resonance (NMR) of the neighbouring nuclei having an shf interaction with the unpaired defect electron. An NMR measurement is not possible since its sensitivity is too low for the defect concentrations in question, which are usually of the order of 10^{-6} or lower. But by detecting the NMR through the desaturation of a partially saturated ESR transition, the sensitivity can be enhanced by several orders of magnitude. This electron nuclear double resonance (ENDOR) experiment was originally introduced by G. Feher (14). The experiments described and explained below use the stationary ENDOR method introduced by H. Seidel (15). The stationary ENDOR is the more widely applicable technique.

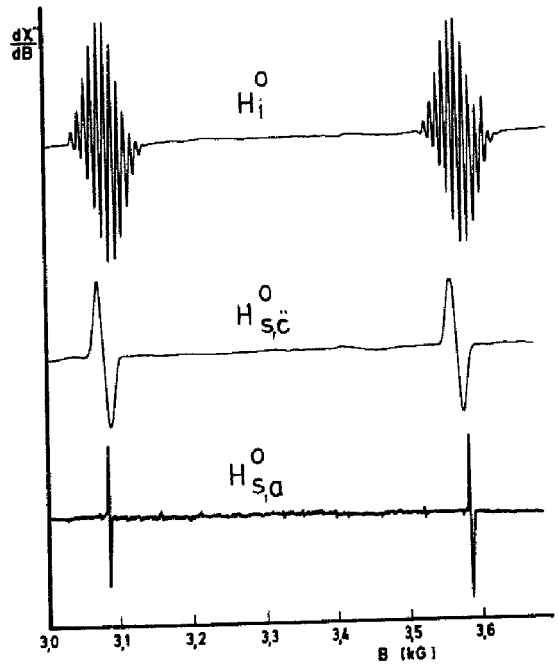

Fig. 9. The ESR spectra of three atomic hydrogen centres in KCl. The hydrogen atoms occupy interstitial sites (H_i^o-centres), anion vacancy sites ($H_{s,a}^o$-centres) and cation vacancy sites ($H_{s,c}^o$-centres). After (13).

Fig. 10 shows for S = 1/2 and one nucleus with I = 3/2 schematically the allowed ESR transitions with resolved shf structure of the ESR. In an ENDOR experiment one of the allowed ESR transitions is partially saturated, that is one chooses the microwave power high enough, so that the transition probability $W_{MW} \propto \gamma B_1^2$ is of the order or larger than the spin lattice relaxation rate $W_{REL} \propto 1/T_1$. γ is the gyromagnetic ratio of the electron, B_1 the microwave field amplitude, T_1 the spin lattice relaxation time. If that is the case, then the spin population of the levels connected by the microwave transition deviates from the Boltzmann equilibrium distribution. If $W_{MW} >> W_{REL}$, then these levels become equally populated. This results in a decrease of the observable microwave absorption, since

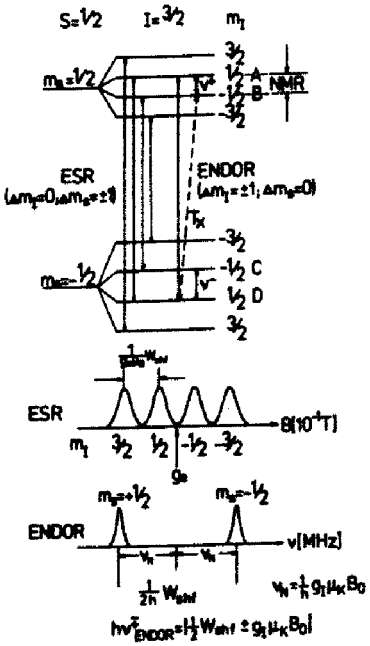

Fig. 10. Level diagram to explain the ENDOR mechanism (see text).

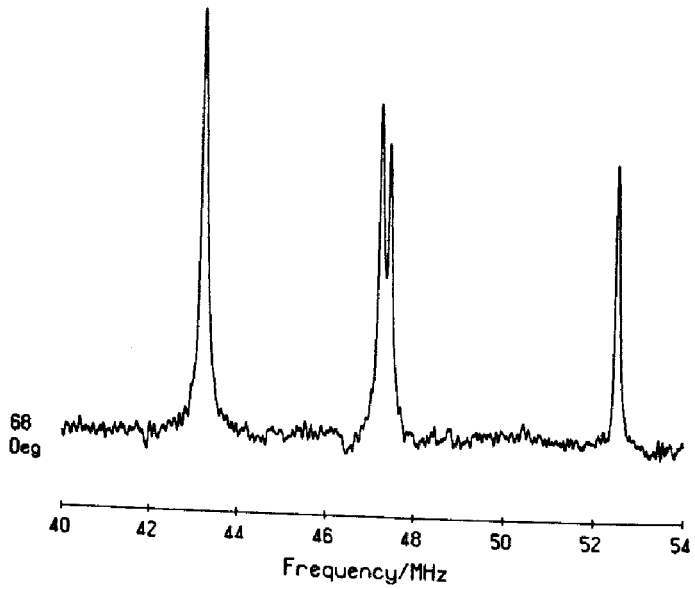

Fig. 11. ENDOR lines of the nearest ^{19}F neighbours of $F(Cl^-)$ centres in SrFCl.

microwave absorption and emission probabilities are equal. The levels not connected by the microwave transitions are not affected. Therefore, e.g. the level population $m_S = +1/2$, $m_I = +1/2$ is now inverted with respect to the level $m_S = +1/2$, $m_I = -1/2$ (see Fig. 10). If these two levels are connected by an NMR transition, the level populations can be equalised, which results in a population decrease of the level $m_S = +1/2$, $m_I = +1/2$ leading to a desaturation of the (partially) saturated transition $m_S = -1/2$, $m_I = +1/2$ to $m_S = +1/2$, $m_I = +1/2$. This desaturation is monitored. It occurs for two NMR frequencies in the example of Fig. 10, since the NMR frequencies for $m_S = +1/2$ and $m_S = -1/2$ are different (see below). Thus, each nucleus gives rise to 2 ENDOR lines (for S = 1/2). A cross-relaxation T_x (see Fig.10) allows the stationary observation of the desaturation (Stationary ENDOR (15)). If several nuclei with the same or similar shf interactions are coupled to the unpaired electron, then the ESR pattern becomes complicated and the shf structure is usually not resolved any more. In ENDOR all nuclei with the same interaction give rise only to two (for S- 1/2) ENDOR lines, which greatly enhances the resolution. ENDOR lines as NMR lines are typically 10-100 kHz wide, about two or three orders of magnitude narrower than the inhomogeneous ESR lines. Thus, in ENDOR one uses the sensitivity enhancement due to a quantum shift from frequencies of $\sim$ MHz to the microwave frequencies of $\sim$ GHz and the increased resolution power due to the smaller NMR line width and the reduction of the number of lines.

Fig. 11 shows as an example ENDOR lines (ESR desaturation) of the 4 nearest ^{19}F neighbours of $F(Cl^-)$ centres in SrFCl (for $m_S = -1/2$), where the unpaired electron occupies a Cl^- vacancy. The structure model of BaFCl, which has the same structure, is contained in Fig. 21. A similar pattern is measured for $m_S = +1/2$ at frequencies shifted by $2\nu_n$ (^{19}F) to lower frequencies.

If I > 1/2, in addition a quadrupole interaction can occur, which is the interaction between the electric field gradient at the site of the nucleus and its quadrupole moment. The ENDOR spectra are described by the following Spin Hamiltonian (for a one electron system, that is without fine structure)

$$\hat{H} = g\beta_e \vec{B}_o \vec{S} + \sum_l (\vec{S}\,\tilde{A}_l\,\vec{I}_l - g_I\,\beta_n\,\vec{B}_o\,\vec{I}_l + \tilde{I}_l\tilde{Q}_l\vec{I}_l) \qquad 4.1$$

The sum runs over all nuclei interacting with the unpaired electron. For simplicity it is assumed that g is isotropic (which is generally not the case). Q is the traceless quadrupole interaction tensor with the elements

$$Q_{ik} = \frac{eQ}{2I(2I-1)} \left.\frac{d^2V}{dx_i\,dx_k}\right|_{r=0} \qquad 4.2$$

Q is the quadrupole moment, V the electrical potential. The spectra are usually analysed in terms of the quadrupole interaction constants:

$$q = \frac{1}{2} Q_{zz}, \quad q' = \frac{1}{2}(Q_{xx} - Q_{yy}) \qquad 4.3$$

The selection rule for ENDOR transitions is:

$$\Delta m_s = 0, \quad \Delta m_I = \pm 1 \qquad 4.4$$

If the shf and quadrupole interaction is small compared to the electron Zeeman term then the quantisation of the electron spin is not influenced by these interactions and the nuclei are independent of each other. They can be treated separately and the sum in equ. (4.1) can be omitted. In perturbation theory of first order, that is with the conditions

$$|B_{ik}|\,, \quad |Q_{ik}| \ll \left|a \pm \frac{1}{m_s}\, g_I\beta_n B_o\right| \qquad 4.5$$

$$\nu^{\pm}_{ENDOR} = \left|\frac{1}{h}\, m_s\, W_{shf} \mp \nu_n \pm \frac{1}{h}\, m_q\, W_Q\right| \qquad 4.6$$

with the following abbreviations:

$$W_{shf} = a + b\,(3\cos^2\theta - 1) + b'\sin^2\theta\cos 2\delta \qquad 4.7$$

$$W_Q = 3\,\{q(3\cos^2\theta' - 1) + q'\sin^2\theta'\cos 2\delta'\} \qquad 4.8$$

θ, δ and θ', δ' are the polar angles of B_o in the principal shf and quadrupole axis system, respectively.

$$\nu_n = \frac{1}{h}\, g_I\,\beta_n\,B_o \qquad 4.9$$

ν_n is the Larmor frequency of a free nucleus in the magnetic field B_o.

$$m_q = \frac{m_I + m_{I'}}{2} \qquad 4.10$$

m_q is the average between the two nuclear spin quantum numbers, which are connected by the transition.

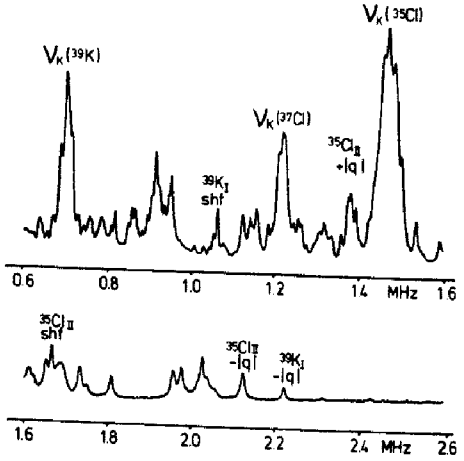

Fig. 12. ENDOR spectrum of $H^0_{s,a}$-centres in KCl. The high field ESR line was saturated (B = 3514 G). T = 40 K, B_0 nearly || to [100]. After (16).

If there is no quadrupole interaction and S = 1/2, then each interacting nucleus gives a pair of lines according to equ. (4.6) ('hf ENDOR-lines'). The lines are separated by $2\nu_n$ if $1/2\ W_{shf} > h\nu_n$ and by W_{shf} if $h\nu_n > \frac{1}{2} \cdot W_{shf}$. If there is a quadrupole splitting, then each 'hf'-ENDOR line is split into a characteristic multiplet, e.g. for I = 3/2 into a triplet. However, this splitting is easily recognised only, if $W_Q << W_{shf}$. If these interactions are of the same order, then the first order approximation leading to equ. (4.6 - 4.8) breaks down. The assignment of particular ENDOR lines to hf or quadrupole transitions becomes difficult.

The chemical nature of a nucleus responsible for a particular hf ENDOR line can usually be determined by measuring the shift of the ENDOR line position when varying the magnetic field B_0 through the ESR line. According to equ. (4.6) and (4.9) the line position varies with ν_n which is proportional to g_I and therefore characteristic for a particular nucleus. Furthermore, in the presence of several magnetic isotopes one can use the repeated appearance of ENDOR lines with a frequency ratio equal to the ratio of nuclear g_I factors.

In Fig. 12 as an example an ENDOR spectrum is shown of atomic hydrogen on anion vacancy sites ($H^0_{s,a}$-centres) in KCl, where several nuclei are identified (ν_K in Fig. 12 = ν_n, the notation I and II stands for first and second neighbour shell). The quadrupole transitions are not recognised easily without a detailed analysis (16).

In order to determine the defect structure and the interaction parameters the dependence of the ENDOR line positions upon variation of the magnetic field with respect to the crystal orientation must be measured and analysed. This is the major problem in an ENDOR analysis and the essential tool for the determination of the defect structure.

Fig. 13 a-c show such an angular dependence for a cubic crystal, such as an alkali halide, calculated according to equ. (4.6 and 4.7) for the first three neighbour shells of a defect on a lattice site. The patterns are characteristic for (100), (110) and (111) 'symmetry' of the neighbour nuclei. For each m_S-value such a pattern is observed. From the number of such patterns according to (4.6) one can infer the electron spin of the defect and thus often its charge state.

Each nucleus has its own principal axis system for the shf and quadrupole tensors. Often, their orientation in a crystal is determined by

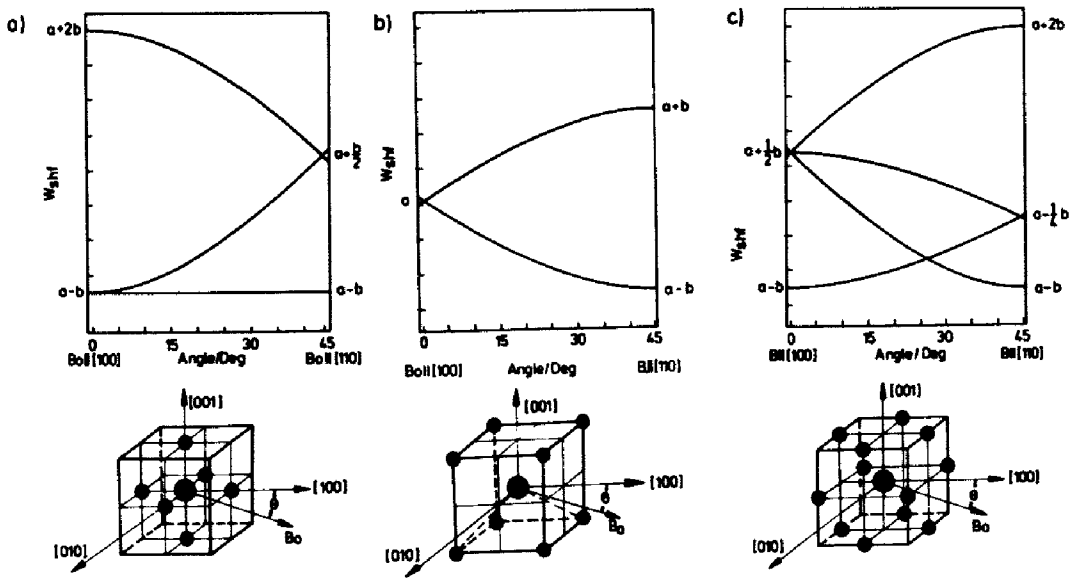

Fig. 13. Calculated ENDOR angular dependence for a defect on a cubic substitutional site. (a) (100)-neighbours, (b) (111)-neighbours, (c) (110)-neighbours.

symmetry. Otherwise, they must be determined from the analysis of the angular dependence of the ENDOR spectra. If the defect centre (impurity) and the respective nucleus are in a mirror plane, then two principal axes must be in this mirror plane. If the connection line between the nucleus and the centre is a threefold or higher symmetry axis, then the tensor is axially symmetric with its axis in this symmetry axis.

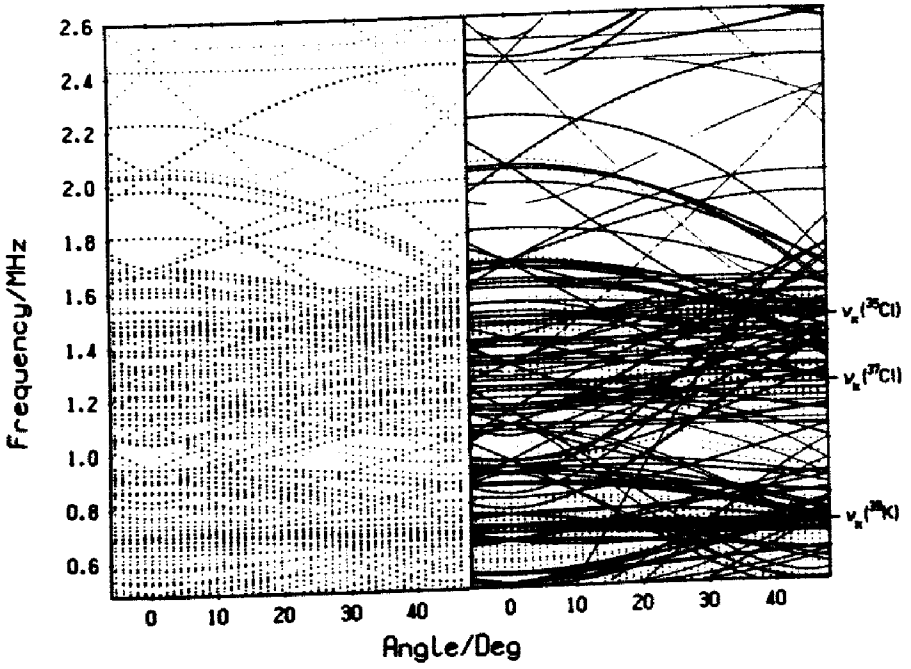

Fig. 14. Angular dependence of the ENDOR lines of $H^{O}_{S,a}$-centres in KCl. The crystal was rotated in a (100)-plane between [100] (0^{o}) and [110] (45^{o}). Left: experimental results. Right: calculated angular dependence after determination of the Spin Hamiltonian parameters for 4 neighbour shells in comparison to the experimental results. Sfter (16).

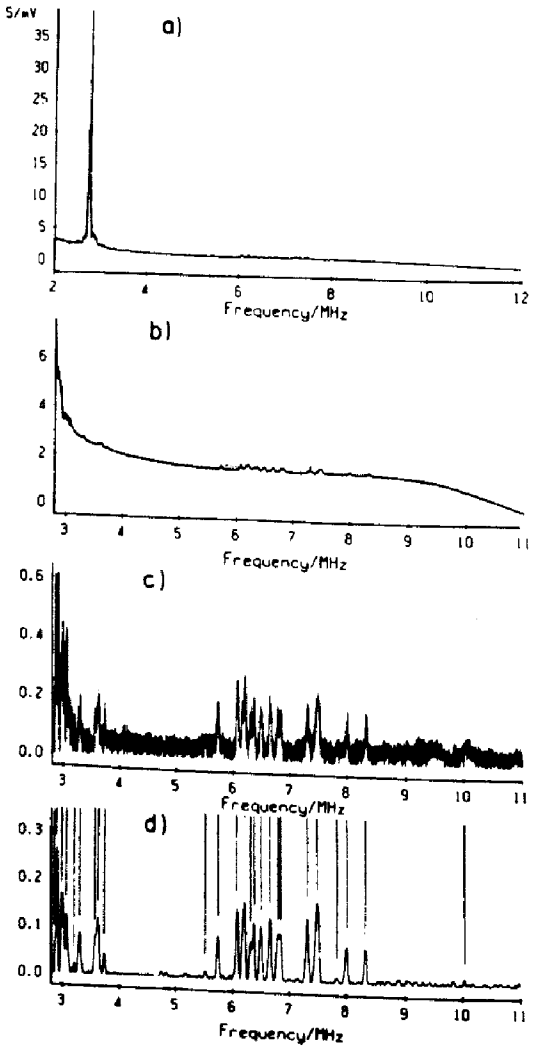

Fig. 15. Digital data processing for an ENDOR spectrum of Fe_i^o-centres in Si. (a) spectrum as measured, (b) subtraction of the strong distant ENDOR at ν_n (^{29}Si), (c) subtraction of a smooth underground line, (d) digital filtering and application of the peak search algorithm (for details see text).

If the angular patterns are separated in frequency, they are easily recognised and the analysis is fairly straightforward. In practice, one usually assumes a model for the defect and then tries to explain the ENDOR angular dependence on the basis of that model. However, both experiment and analysis become often very difficult due to the following complications. One is that many angular patterns overlap strongly in a narrow frequency. range. This is the case for the $H_{s,a}^o$-centres in KCl, as seen from Fig. 14. The angular pattern can become complicated due to the many centre orientations of low symmetry defects and due to the fact, that the simple solution of first order of the Spin Hamiltonian breaks down. The angular dependence can be calculated by a complete diagonalisation of the Spin Hamiltonian and the analysis is performed as a fit procedure between the experimental data and the calculated angular dependencies. The result of this is seen in Fig. 14 for the $H_{s,a}^o$-centres (16). If the fit agrees with the experimental data, the analysis is unambiguously correct. There are many more experimental points than parameters to be extracted from them. The number of ENDOR lines can be very high. As an example, the Ni^{3+} centre in GaP may be mentioned, where for each field orientation over 600 ENDOR lines were observed (17). Because of this, with conventional ENDOR spectrometers only comparatively simple problems could be solved. In recent years considerable progress was made by setting up computer controlled ENDOR spectrometers and by using computers for the data processing and analysis of the spectra.

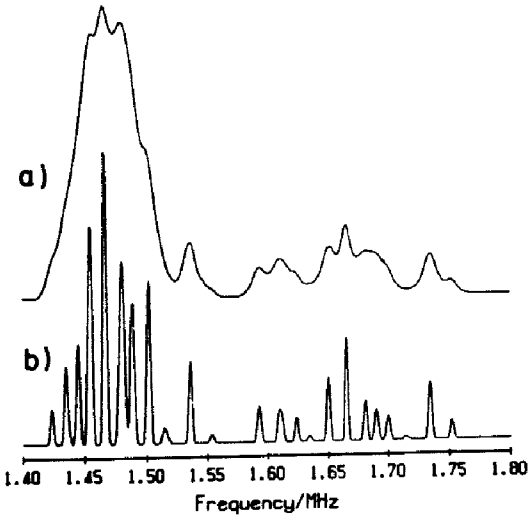

Fig. 16. Deconvolution of spectra to enhance the resolution of ENDOR, (a) section of the spectrum of Fig. 14, (b) after application of the deconvolution program. After (19).

The angular dependence must be measured in small angular steps and due to the low signal to noise repeatedly many times. In the computer controlled ENDOR spectrometer the computer controls the following experimental parameters: rf (NMR frequencies), magnetic field, crystal orientation, sample temperature and cavity matching. Thus, the angular dependence can be measured automatically, also as a function of temperature. A full angular dependence can take up to 2-3 weeks of continuous measurement. The ENDOR lines are stored in the computer and with a specially developed software (see below) their positions can be determined automatically and a computer plot of the angular dependence can be made. Fig. 14 is such a plot.

The application of digital methods to the processing of the experimental data is summarized in Fig. 15 for the example of interstitial Fe_o centres in Si (18). Fig. 15a shows the ENDOR lines of interest between 6 and 8 MHz, which are very weak compared to the 'distant ENDOR' due to the free ^{29}Si nuclei and to a strong underground signal. The latter and the distant ENDOR must be subtracted in order to deal better with the lines of interest. With a special algorithm the underground is subtracted. It does not assume a particular form of the underground. It 'eliminates' the sharp peaks from the rest, which then is subtracted from the total spectrum (19). The resulting spectrum is that of Fig. 15c, which contains a number of ENDOR lines and, of course, noise. The signal to noise ratio of ENDOR spectra is usually not too good. The ENDOR effect in solid state defects is mostly below 1% of the ESR signal. Low defect concentration and the limited ENDOR effect are the major reasons for the poor signal to noise ratio. Here the use of digital filtering has proved to be very advantageous. The major ideas behind this are the following: what is wanted is a smoothing of the spectra without disturbing the signals. Conventional RC-filters have a poor trade-off between noise reduction, signal distortion and speed of measurement. A simple digital method would be a running average algorithm, which replaces a data point by the average of the original data point and its unfiltered left and right neighbour points. This symmetric average over (2 N + 1) data points produces the classic noise reduction of any averaging process of uncorrelated data. This idea can be improved by assinging different weights to the neighbouring data points.

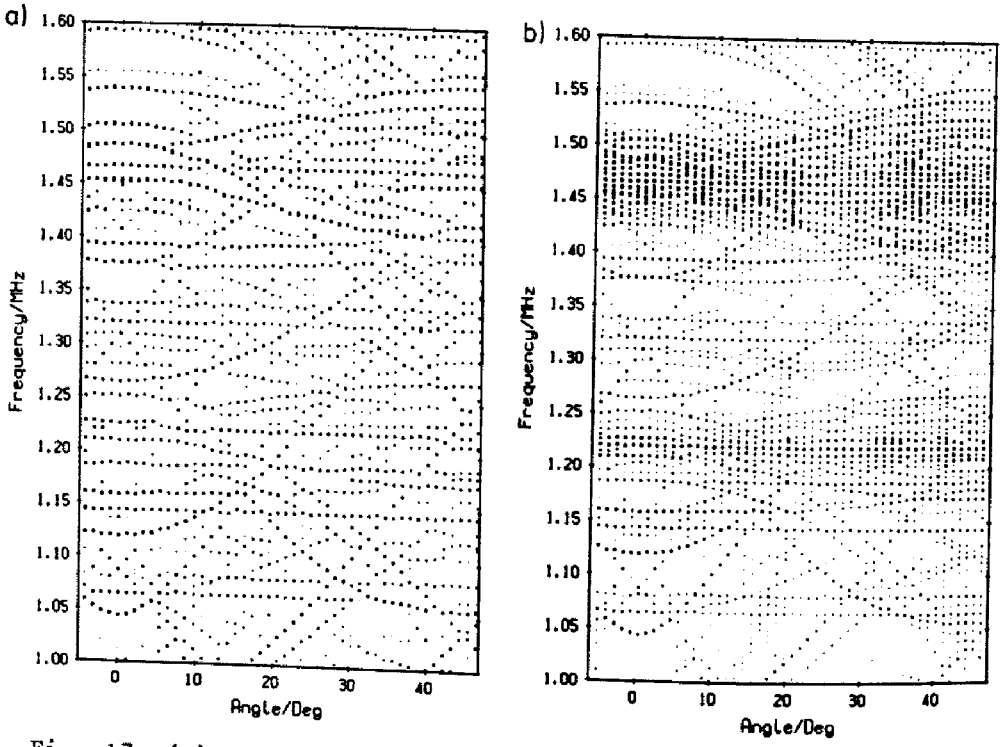

Fig. 17. (a) Section of the ENDOR angular dependence of Fig. 14 ($H^{o}_{s,a}$-centres in KCl), (b) the same section after application of the deconvolution program. After (19).

$$f[K] = \sum_{i=-N}^{N} a[i] \cdot Y[K-i] \qquad 4.11$$

Here Y denotes the unfiltered and f the filtered data points. The weights a[i] describe the digital filter used. For a simple running average one has

$$a[i] = {}^{1}/_{(2N+1)} \qquad 4.12$$

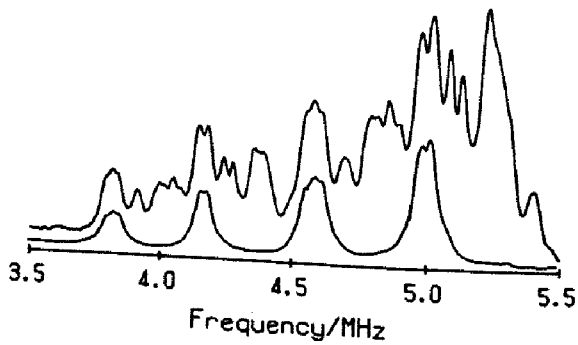

Fig. 18. Lower trace: section of the ENDOR spectrum of F centres in KCl:F^{-} prior to conversion to $F_H(F^{-})$ centres. The lines are due to second shell ^{37}Cl and ^{35}Cl nuclei. Upper trace: the same section after conversion of about 50% F centres into $F_H(F^{-})$ centres. After (26).

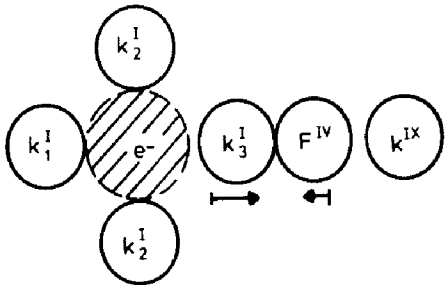

Fig. 19. Model of $F_H(F^-)$ centres in KCl as derived from the ENDOR analysis.

If one requests, that the filtering process conserves additive constants, linear slopes, and parabolic peaks, area, first, second and third moments and minimises noise under these constraints, it can be shown that the weight function

$$a[i] = 3\ ((3N^2 + 3N - 1) - 5i^2)/((2N-1)\cdot(2N+1)(2N+3) \qquad 4.13$$

is optimal for any line shape (20). Such a filter is called DISPO filter (digital smoothing with polynominal coefficient) (21). Compared to an RC-filter it typically decreases the signal distortion by a factor of 20. For small signal distortion (1%) and equal scan speed it reduces the noise by an additional factor of 5 compared to the RC-filter (22,23).

Fig. 15d shows the application of such a filter to the spectrum of Fig. 15c. The line positions are determined by a special peak search algorithm, in which the 2nd derivative of the smoothed spectrum is calculated. A peak is, where this has a local minimum (19). This is exact for symmetrical ENDOR lines of Gaussian or Lorentzian shape. The measurement must make sure that the line shape remains symmetrical for this to be applied. Therefore, for this kind of ENDOR spectroscopy, the method of 'transient ENDOR' originally introduced by G. Feher (14) is not applied, since there the line shapes are nonsymmetrical.

When too many ENDOR lines overlap, the application of the peak search algorithm is not sufficient. An improvement can be reached by applying a deconvolution algorithm, which decomposes the spectra in an iterative process, since the exact shape and width of the single ENDOR lines are not known beforehand.

Fig. 16a shows a section of the spectrum of Fig. 12. After the application of the deconvolution procedure one obtains Fig. 16b. In Fig. 17a and 17b the ENDOR angular dependence of $H^o_{s,a}$-centres in KCl with and without application of the deconvolution is compared. Clearly visible is in the section between 1.45 - 1.50 MHz and 1.20 - 1.25 MHz the advantage of this procedure. The angular dependence can be followed much better and can be analysed. The analysis yields as the site for the H^o atom the anion vacancy, the values of the shf and quadrupole interaction constants given in table 1 as an example for typical ENDOR results. The Spin Hamiltonian had to be diagonalised numerically (16).

Table 1. Shf and quadrupole constants of $H^{o}_{s,a}$-centres in KCl (in kHz), (T = 40 K). After (16)

shell	constant	$H^{o}_{s,a}$
$^{39}K_{I}$	a	253
	b	219
	q	198
$^{35}Cl_{II}$	a	57
	b	312
	b'	-3
	q	-88
	q'	-94
$^{35}Cl_{IV}$	a	37
	b	54
	q	±45
$^{39}K_{V}$	a	4
	b	11
	b'	≈0
	φ_B	26.0^{o} $\pm 0.2^{o}$
	q	±39
	q'	±17
	φ_Q	13.5^{o} $\pm 0.2^{o}$

The interaction constants are uncertain to ±1 kHz. φ_B, φ_Q = ∢(z, [100]).

Not always it is possible to unambiguously determine the defect structure by the analysis of the ENDOR angular dependence. In crystals with high symmetry as silicon or III-V semiconductors, like GaP, with a diamond and zinc blende structure, respectively, there is a particular difficulty. With respect to the substitutional site and the interstitial site with T_d symmetry, there are the same kind of neighbour shells with the same occupancy with (100), (110) or (111) symmetry. Only the sequence is different. However, from the experiments alone one can only determine the symmetry type of a neighbour nucleus and not say which distance it has from the centre. This would require a knowledge of the wave function Ψ or at least how it varies with distance from the defect centre. If this was known, an estimateof the interaction parameters would allow a shell assignment of the measured nuclei according to equ. (3.9), (3.10) and (4.2). If this is not known, then one cannot distinguish between the two sites. This difficulty came up recently when investigating Te^{+} and Se^{+} centres in Si (24, 25) and Ni^{3+} centres in GaP (17). In ionic solids one can usually assume that $\psi(r)$ falls off monotonically with distance and therefore difficulties in assigning neighbour nuclei usually do not occur. This is generally not the case in semiconductors, where oscillations of the wave functions can occur, also for deep level defects.

Photochemical reactions of point defects can also be studied by ENDOR. As an example the conversion of F centres in KCl into $F_H(F^-)$ centres by bleaching the optical F centre absorption band in KCl doped with F at a temperature where the anion vacancies are mobile is shown in Fig. 18. In the lower trace a section of the second shell Cl ENDOR spectrum of the F centres prior to the conversion is shown, above the same section after conversion of about 50% of the F centres into $F_H(F^-)$ centres. New ENDOR lines appear between the original ones. In ESR the new centres cannot be

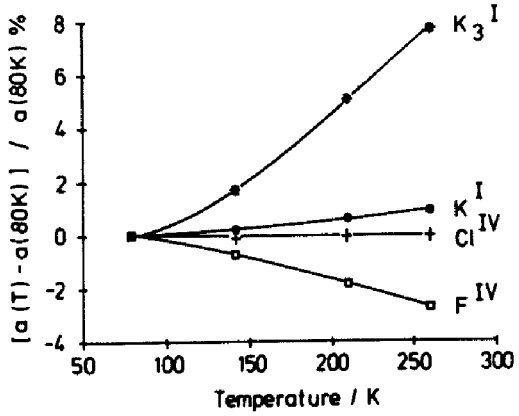

Fig. 20. Temperature dependence of the isotropic shf constant a of K_3^I and F^{IV} neighbours of $F_H(F^-)$ centres compared to the corresponding temperature dependence of a of K^I and Cl^{IV} neighbours of F centres.

distinguished from the F centres. Fig. 19 shows the structure model derived from the analysis of the $F_H(F^-)$ spectrum (26). F^- occupies a 4th shell position and not a 2nd shell position as may have been assumed. A separation of the ENDOR spectra can be difficult if the 'old' spectrum is only partially converted and overlaps strongly the 'new' one. There are, however, methods to separate these ENDOR spectra, as will be shown in the following sections.

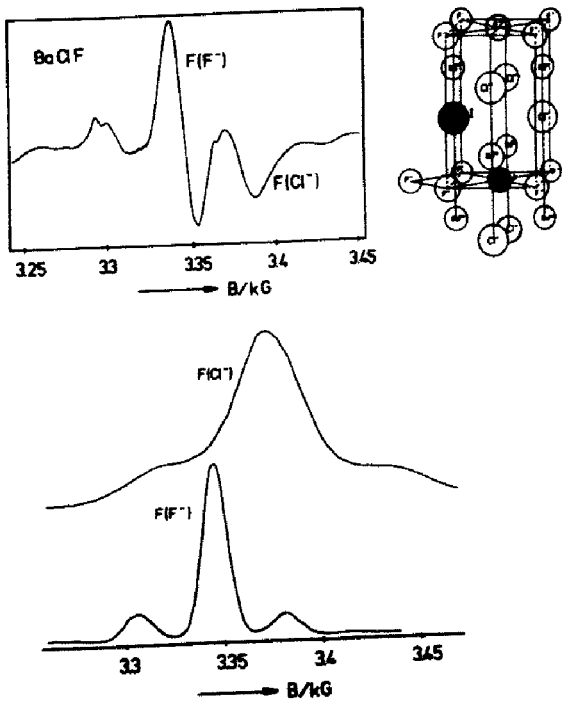

Fig. 21. Model of the two F centres in BaFCl ($F(Cl^-)$ and $F(F^-)$ centres), their superimposed ESR spectra (derivative) and the ENDOR-induced ESR spectra of both centres measured using a ^{19}F ENDOR line of each centre. After (32).

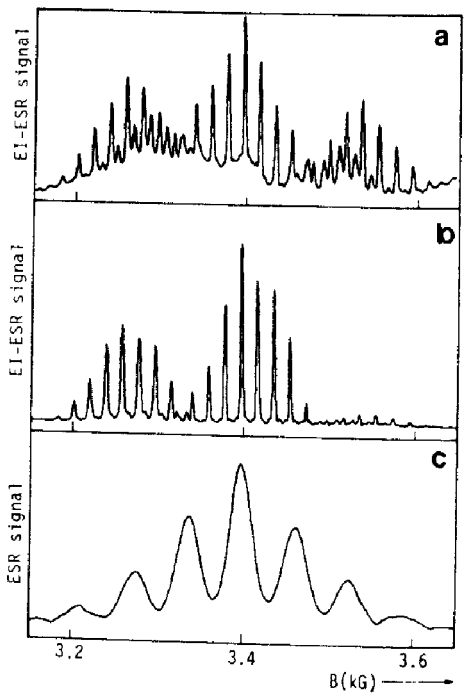

Fig. 22. ESR and ENDOR-induced ESR spectrum of X-irradiated $KMgF_3$ doped with Fe^{2+}, (a) integrated ESR spectrum after X-irradiation at room temperature, $B_0 \| [100]$, (b) ENDOR-induced ESR spectrum for the ^{19}F ENDOR line at 42.5 MHz. The spectrum is due to Fe^{3+}, (c) ENDOR-induced ESR spectrum for the ^{19}F ENDOR line at 21.0 MHz. The spectrum is due to F centres. After (34).

With ENDOR also dynamical properties of defects can be studied by measuring the temperature dependence of the ENDOR line positions. Since each ENDOR line position can be determined with high precision (to 1-10 kHz, depending on the line width), also comparatively small effects can be seen. In Fig. 20 the temperature dependence of the isotropic shf interaction constant of K_3^I (see Fig. 19) and F^{IV} neighbours of $F_H(F^-)$ centres

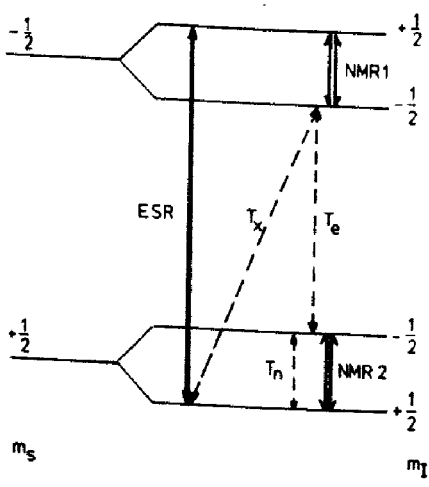

Fig. 23. Level scheme to explain the special tripel resonance experiment (DOUBLE ENDOR) (see text).

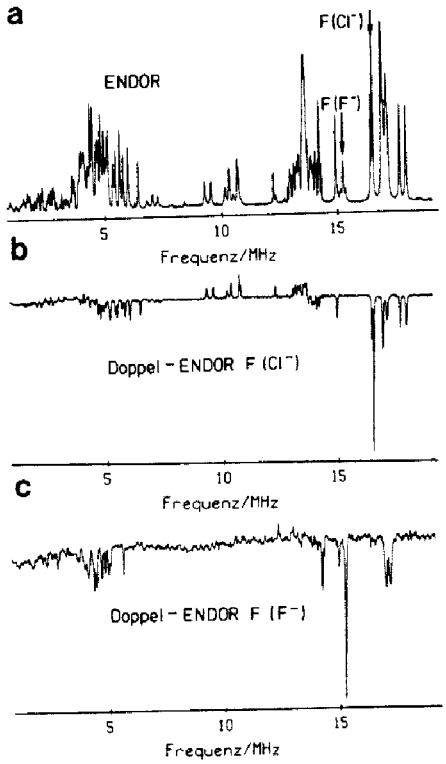

Fig. 24. (a) Part of the ENDOR spectrum of $F(Cl^-)$ and $F(F^-)$ centres simultaneously present in BaFCl, (b) ENDOR spectrum for setting one ENDOR frequency to an ENDOR line of $F(Cl^-)$ centres (see mark in Fig. 24a), (c) DOUBLE ENDOR spectrum for setting one ENDOR frequency to an ENDOR line of $F(F^-)$ centres (see mark in Fig. 24a). After (37).

and of the corresponding K^I and Cl^{IV} neighbours in F centres is plotted between 77 and 300 K (27). The strong temperature dependence of K_3^I of $F_H(F^-)$ reflects that K_3^I, which is displaced by 11% towards F^-, has more room compared to K^I in the F centre and experiences a large local mode vibration, while F^{IV} is knocked further away through these vibrations.

Another example is the strong temperature dependence of the shf interaction observed for atomic hydrogen centres on anion or cation sites (16, 28,29), which have local vibrational modes with very high amplitudes due to the light hydrogen mass.

In crystals with structural phase transitions the lattice changes its symmetry at T_c. This can be 'seen' by a paramagnetic probe, which therefore can be used to study such transitions. A recent example is the investigation of Mn^{2+} in $RbCdF_3$, which goes at 124 K from a cubic to a tetragonal phase. With ENDOR it was possible to study the order parameter as a function of temperature, which is directly reflected in the splitting of the ENDOR lines with temperature upon going through T_c for suitable field orientations. It turned out that the order parameter measured is smaller than the intrinsic value, since the lattice relaxes around the probe and this 'decouples' it from the lattice somewhat (30,31).

5. ENDOR-INDUCED ESR

Overlapping ESR spectra of different defects cause overlapping ENDOR spectra. It can be very difficult if not impossible to analyse their angular dependence, especially if many ENDOR lines occur in a narrow

frequence range. Furthermore, there may be weaker ESR spectra buried under stronger ones having observable ENDOR lines, which can be analysed, but the ESR spectrum cannot be measured. The two type of F centres possible in BaFCl, e.g. are produced simultaneously. Their ESR spectra strongly overlap (see Fig. 21). In such a case one can measure a kind of excitation spectrum of a particular ENDOR line belonging to one defect, which gives an image of the corresponding ESR spectrum belonging to the same defect (ENDOR-induced ESR-spectrum). This can be seen from Fig. 10. The ENDOR transitions can be measured by setting B_o to either of the 4 shf ESR transitions for m_I = 3/2, 1/2, -1/2 and -3/2, thus the ENDOR line intensity measured should follow the ESR line pattern in the middle of Fig. 10. According to equ. (4.6), however, the frequency of an ENDOR line depends on ν_n and therefore on B_o. Because of this one must 'correct' the ENDOR frequency for the variation of B_o when going through the ESR-spectrum. This can easily be done with the computer controlled spectrometer in other ways provided the corresponding nuclear g_I factor is known. In measuring the ENDOR-induced ESR spectrum one monitors the ENDOR line intensity of a particular ENDOR line, while varying the magnetic field through the ESR spectrum and correcting the frequency position according to equ. (4.6). The resulting spectrum is an image of the (integrated) ESR spectrum of that defect, to which the ENDOR line (nucleus) belongs. In this way the ESR spectrum of different defects can be separated.

Fig. 21 shows this for the 2 F centres in BaFCl. The two ENDOR-induced ESR spectra were measured using ^{19}F ENDOR lines of both centres. For S = 1/2 and no quadrupole interaction experienced by the nucleus taken for the measurement, the ENDOR-induced ESR spectrum corresponds to the true ESR line shape, if the cross relaxation does not depend on m_I and is the dominating electron spin relaxation process. This was observed in several cases (32).

If the transition used is a quadrupole ENDOR line then not the true ESR lines are measured with the ENDOR-induced ESR spectrum. The deviations can, however, be minimised, if one choses an ENDOR line with a very small interaction, that is near the Larmor frequency ν_n of the nucleus. For details see (32,33).

For systems with S > 1/2 there is usually a fine structure interaction splitting of the electron Zeeman levels. Then in ENDOR-induced ESR one measures only some of the possible ESR transitions. This is demonstrated for Fe^{3+} centres in $KMgF_3$, which were produced by X-irradiation of $KMgF_3$ doped with Fe^{2+}. In Fig. 22a the integrated ESR spectrum of the 5 ESR transitions is reproduced with partly resolved shf structure with six nearest ^{19}F neighbours. Fig. 22b shows the ENDOR-induced ESR spectrum measured with a ^{19}F ENDOR line at 42.5 MHz displaying 2 of the five Fe^{3+} ESR transitions, while Fig. 22c shows the ENDOR-induced ESR spectrum measured with a ^{19}F ENDOR line at 21.0 MHz. Clearly, another ESR spectrum appears. It was buried under the Fe^{3+} spectrum beyond recognition and turned out to be due to simultaneously produced F centres (34). A detailed analysis also allows the determination of the relative signs of quadrupole interaction constants, shf interaction constants and fine structure constants (32,33).

6. DOUBLE ENDOR

Although with ENDOR-induced ESR experiments each ENDOR line can be 'labelled' to a particular defect in case of the simultaneous presence of several defects, this can be a tedious task, especially if one has to follow a complicated angular dependence. Such a situation is usually encountered in radiation damage studies. Therefore, a method is called

for with which the ENDOR spectra of different defects can be measured separately. This can be done by measuring a triple resonance, in which 2 NMR frequencies are applied simultaneously together with the microwaves. The simplest case, the so called 'special triple resonance' (special DOUBLE ENDOR) is schematically shown in Fig. 23 for the simple case of $S = 1/2$, $I = 1/2$. If stationary ENDOR is measured for the transition 'NMR1' between $m_s = -1/2$, $m_I = 1/2$ and $-1/2$, then the signal height is determined by the ESR transition probability (that is by B_1^2), the NMR1 transition probability (that is B_{rf}^2 (NMR1)) and the cross relaxation time T_x. It is assumed (and a condition for the experiment), that $T_x > T_e$, the electron spin lattice relaxation time, due to the comparatively long nuclear spin lattice relaxation time T_n. If then a second rf frequency is applied between the levels $m_s = 1/2$, $m_I = 1/2$ and $-1/2$ (NMR2) then T_n is effectively shortened by this transition and therefore T_x is also shortened, which results in an enhancement of the monitored ENDOR signal at the frequency NMR1. In the experiment one irradiates with the fixed ENDOR frequency NMR1, monitors the ENDOR line intensity of the line at NMR1, while sweeping the second rf frequency. When the transition NMR2 is induced the ENDOR line intensity NMR1 increases. The increase is the DOUBLE ENDOR signal and is deteced with a double lock-in technique.

In the stationary DOUBLE ENDOR spectrum positive and negative signals are observed (35,36). Negative signals occur if the second NMR frequency is induced between nuclear states belonging to the same m_s quantum number. Fig. 24 shows the DOUBLE ENDOR spectrum for the two F centres in BaFCl. In Fig. 24a the ENDOR lines of both F centres are superimposed, a full analysis was not possible. In Fig. 24b the fixed ENDOR frequency NMR1 was set to one ENDOR line belonging to $F(Cl^-)$ centres and NMR2 was swept between 1 and 19 MHz and the DOUBLE ENDOR effect was recorded. In Fig. 24c the analogous experiment was made for an $F(F^-)$ ENDOR line. Both DOUBLE ENDOR spectra show only lines due to the $F(Cl^-)$ or $F(F^-)$ centres alone. Especially around 5 MHz both centres have many ENDOR lines, which otherwise could not have been separated (37).

DOUBLE ENDOR is also very important to analyse low symmetry defects. The defects are distributed over several orientations in the crystal. The ESR and ENDOR spectra of these orientations overlap. In a sense each defect orientation is equivalent to a new defect species. With DOUBLE ENDOR the spectra of one particular defect orientation can be measured separately, which greatly facilitates the analysis or makes it at all possible. In a recent investigation of O^- centres in α-Al_2O_3, which had very low symmetry (that is 'no' symmetry) a definite assignment of the quadrupole ENDOR lines to their corresponding 'hf' ENDOR lines was only possible after one particular centre orientation could be measured separately (38).

7. OPTICALLY DETECTED MAGNETIC ELECTRON SPIN RESONANCE (ODESR)

There are several ways to detect ESR optically. Which of the techniques is applied depends on the system studied and on the kind of question one wants to answer. Compared to 'conventional' ESR the optical detection, if possible, has several advantages with respect to the identification of defects:

(i) higher sensitivity
(ii) higher selectivity
(iii) direct correlation between optical and structural properties
(iv) possibility to investigate optically excited states.

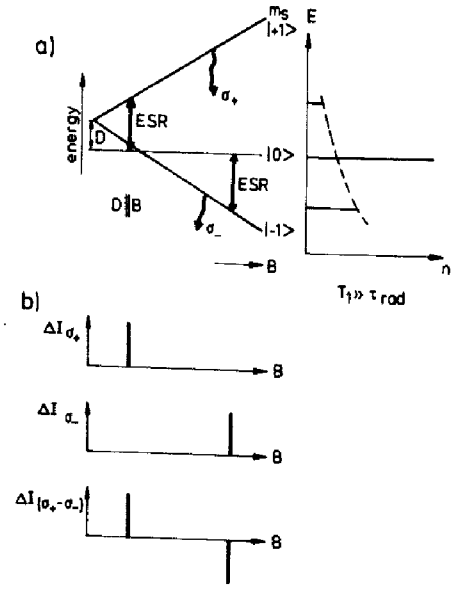

Fig. 25. Level scheme of triplet states to illustrate the optical detection of ESR via a microwave-induced change in the luminescence intensity or via the magnetic circular polarisation of the emission (MCPE). It is assumed that $B_0 \| D_{zz}$, $T_1 >> \tau_{rad}$.

The sensitivity enhancement can be up to 10^4 - 10^5, compared to the conventional ESR, depending on the method used and the physical parameters of the system. The high selectivity is based on the possibility to use single absorption or emission bands for the detection. The bands of different defects usually do not overlap entirely and hence, these defects can be measured separately. A correlation of optical properties with structural property is based on the same argument. Relaxed excited states of sufficient radiative lifetimes can be studied. The condition is, that the microwave transition rate is of the same order or bigger than the reciprocal radiation lifetime. If this condition is not fulfilled, during the lifetime of the state no occupation changes of the Zeeman levels can be induced by the microwaves. ESR spectra of excited states with lifetimes of the order of microseconds have been detected several times. The actual technical limit, which is mainly given by the microwave amplitude to be applied at low temperature, is probably at lifetimes of the order of 100 n sec.

The optical detection of ESR is based on either the observation of a microwave-induced intensity change in luminescence or on the observation of microwave-induced changes of the degree of polarisation of either absorption or emission. A condition is that the Zeeman levels involved are occupied differently and that the radiative transitions differ in polarisation properties. It should be noted that the Zeeman splitting of the levels is only of the order of 10^{-4} eV, while the phonon broadening of the levels due to electron phonon coupling is 3 orders of magnitude bigger (see section 2). Fortunately, the polarisation of the optical absorption or emission transitions is usually only little affected by the phonons, so that microwave-induced population changes within the Zeeman levels can be observed.

The examples and methods discussed below are chosen mainly with respect to defect identification. Not mentioned, e.g. are interesting studies like radiative/nonradiative transitions or electron transfer in excited states for which ODMR is an excellent tool, nor the study of relaxed excited states if the defect model is known from ground state ESR.

Defects with 2 valence electrons, e.g. in a ns^2 configuration, often have relaxed excited triplet states, in which the two electrons have parallel spins and S = 1. The optical absorption leads first to a singlet excited state with S = 0, which then relaxes into the triplet state by intersystem crossing. The two electrons possess then a fine structure interaction (e.g. due to dipole-dipole interaction), so that the Spin Hamiltonian of equ. (3.3) obtains an additional term

$$\underset{\sim}{H}_{FS} = \vec{\underset{\sim}{S}}\ \tilde{D}\ \vec{\underset{\sim}{S}} \qquad 7.1$$

In perturbation theory of first order the energy is given for an axially symmetric fine structure tensor and B_o parallel to its principal axis (then $D_{zz} = D$)

$$E_{FS} = D\ [m_s^2 - \frac{1}{3} \cdot S\ (S + 1)] \qquad 7.2$$

Fig. 25 shows the level scheme as a function of the magnetic field of the Spin Hamiltonian containing the term 7.1 and the electron Zeeman interaction. The three levels are all occupied from a higher singlet state. Raditative transitions from the triplet states into the singlet ground states are forbidden. However, the states $|+1\rangle$ and $|-1\rangle$ can mix with excited singlet states via the spin orbit interaction and therefore a finite raditative transitions probability into the ground state is observed for these levels, while $|0\rangle$ cannot decay by radiative transitions. The radiative lifetime of the $|+1\rangle$ and $|-1\rangle$ levels depends on the size of the spin orbit interaction and the energy separation of excited singlet states from the triplet state.

Due to the radiative decay of the $|+1\rangle$ and $|-1\rangle$ levels, these levels are less populated in a stationary state compared to the level $|0\rangle$, where population is accumulated (see Fig. 25). It is assumed that the spin lattice relaxation time T_1 is large compared to the radiative lifetime.

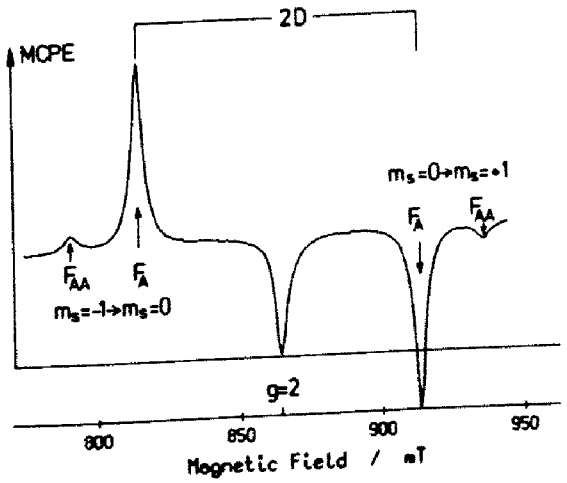

Fig. 26. Magnetic circular polarisation of the emission (MCPE) recorded at λ>700 nm under cw-microwave irradiation (24 GHz) as a function of magnetic field ($B_o \| [100]$ in CaO containing F_A(Mg) and F_{AA}(Mg) centres. T = 1.6 K. After (41).

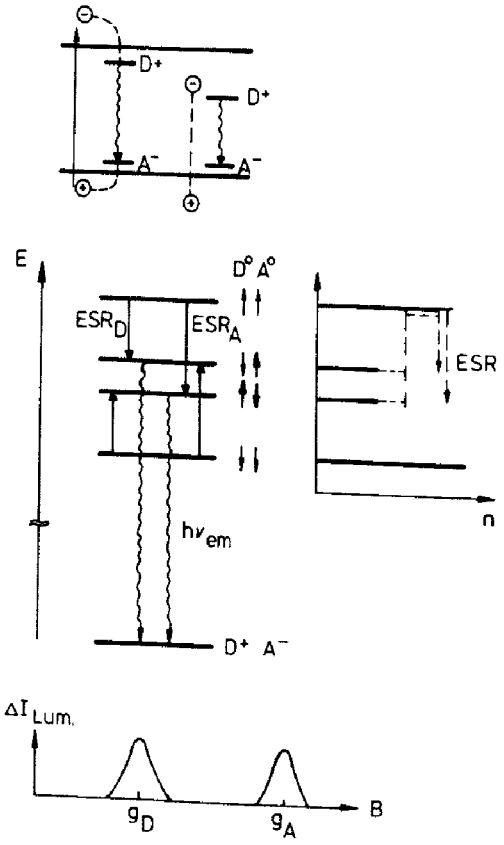

Fig. 27. Schematic representation of donor-acceptor recombination in semiconductors and of the mechanism to observe ESR as a change in intensity of the donor-acceptor recombination luminescence.

Therefore the microwave transtion $|0\rangle \rightarrow |+1\rangle$ and $|-1\rangle \rightarrow |0\rangle$ shift population into the radiative levels, upon which the luminescence intensity is enhanced. This can easily be observed. On the other hand, one can also observe the magnetic circular polarisation of the emission ($I_{\sigma+} - I_{\sigma-}$) (MCPE), where for the low field transition an enhancement, for the high field transition a decrease is observed. (See Fig.25b, where D > 0 is assumed).

F centres in CaO, where an O^{--} vacancy is occupied by two electrons, do have such relaxed excited triplet states and their ODESR was observed in such a way (39,40). Fig. 26 shows as an example the ESR spectrum of F_A and F_{AA} centres in CaO doped with Mg^{++} observed at λ>700 nm (1). Both centres differ slightly in their fine structure constant D. Measurements with higher resolution show a shf interaction with the 10% abundant ^{25}Mg (I = 5/2). Six equidistant shf lines can be resolved (40,41). In the F_A centre there is one Mg^{++} next to the O^{--} vacancy, in the F_{AA} centre two Mg^{++} opposite each other along a (100) axis.

In semicoductor physics the observation of ODESR in the donor-acceptor recombination luminescence plays a very important role for defect identification. The fundamental process is illustrated in Fig. 27. Upon an optical band-band transition an electron-hole pair is created. The electron is captured by an ionised donor D^+ and the hole by a negatively charged acceptor A^- (semi-insulating or p-type semiconductor) according to

$$D^+ + A^- + e^- + h^+ \rightarrow D^o + A^o \qquad 7.3$$

Both D^0 and A^0 are paramagnetic. The unpaired electron at the donor and the unpaired hole at the acceptor can recombine under emission of a luminescence radiation

$$D^0 + A^0 \rightarrow D^+ + A^- + h\nu \qquad 7.4$$

The level scheme of D^0 and A^0 in a magnetic field is shown in Fig. 27. The two spins are assumed to be very weakly coupled (42). The energy positions of the levels are therefore determined only by their respective g-factors and the magnetic field. Since from the two triplet states a radiative decay into the singlet ground state is forbidden, only from the two singlet states, where the two spins are antiparallel, a luminescence is observed. Therefore, in a stationary state, the population of the two triplet states is higher compared to the two singlet states, similarly as discussed above for the state $|0\rangle$ in the highly coupled triplet system.

Upon the microwave transitions indicated in Fig. 27 the recombination luminescence is increased and in principle one can observe the ESR lines of both the donor and acceptor provided their g-factors are different enough. Usually, one observes only the donor resonance since the p-type hole states of the acceptors experience a dynamical Jahn-Teller effect with the consequence that the resonance is very difficult to observe. It can be observed upon application of uniaxial stress if this is sufficiently large to suppress the dynamical Jahn-Teller effect.

With this technique recently the ODESR of anion antisite defects in GaP:Zn (p-type) could be observed. Upon band-band excitation two strongly overlapping luminescence bands can be observed, one peaking at 0.95 eV, the other at 1.20 eV. In the 0.95 eV luminescence a doublet ODESR spectrum is observed, which is due to a P atom on a Ga site ('antisite') with one unpaired electron. The doublet splitting is due to the hf interaction with the ^{31}P nucleus (I = 1/2)(43,44). Using a specific modulation technique also the shf interaction with 4 nearest ^{31}P-neighbours could be resolved from which the structure model could be inferred (43). The acceptor resonance could not be seen.

Fig. 28 shows the ODESR spectrum measured in the 1.20 eV luminescence, which is also due to an antisite defect, however, in a triplet state and

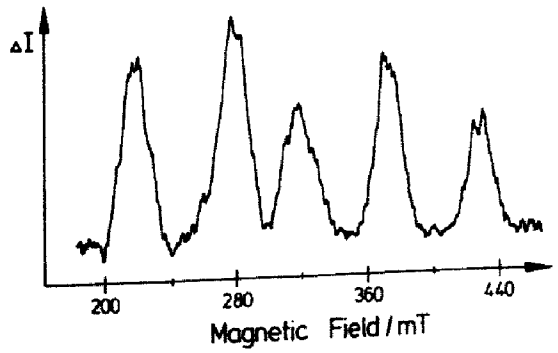

Fig. 28. X-band ODESR spectrum observed as a microwave-induced change of the donor-acceptor recombination luminescence in GaP:Zn (excitation wavelength 514 nm). The spectrum shows the donor PP_3Y_P in a triplet state and the acceptor (central line) which is probably Fe_i^{3+}. $B_0 \| [111]$. After (45).

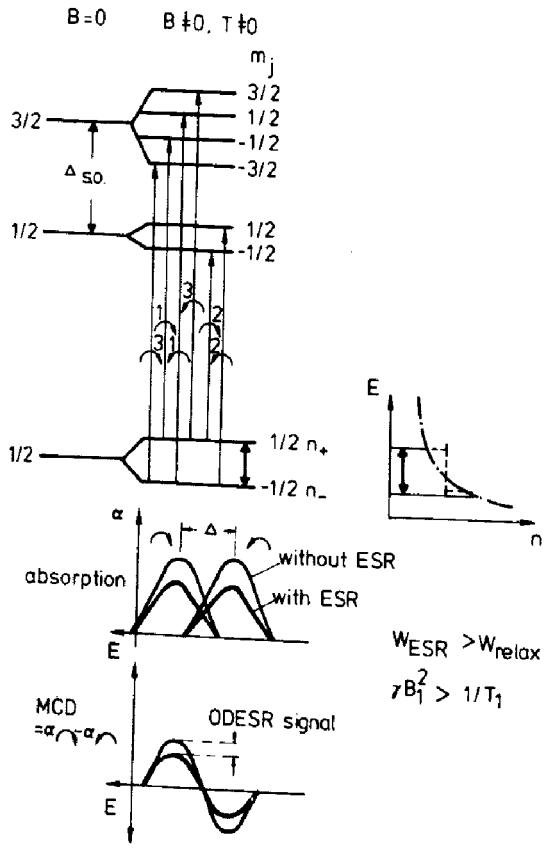

Fig. 29. Simple model to explain the magnetic circular dichroism (MCD) of the absorption and its microwave-induced decrease to detect the ESR transitions.

which also contains the ESR line of the acceptor taking part in the luminescence process. The two low and high field lines are due to the antisite, the splitting between the two lines of each doublet is due to the ^{31}P hf interaction, while the separation of the centres of the two doublets (between approx. 240 and 400 mT) corresponds to the separation of the lines in Fig. 26 and is due to the fine structure interaction. It was concluded that the structure model is a PP_3Yp defect with an unknown atom on one of the 4 nearest neighbour P sites and that the acceptor may be a nearby interstitial Fe^{3+} impurity (45). The level of the defect is at E_V + 1.5 eV. The PP_3Yp defect can be excited into its triplet state by direct excitation from the valence band with sub-band gap light, a possibility also indicated schematically in Fig. 27. This excitation enhances the luminescence, since the defects can be excited in the bulk of the crystal and not only in a thin surface layer, as is usually the case for band-band transitions due to the high absorption constant. When measuring the ODESR via recombination luminescence one common difficulty is, that there is a distance distribution between donors and acceptors and that the exchange interaction between them can be large and varying according to distances. It is especially large for shallow donors and acceptors. This results in a broadening of the ESR lines. Therefore, in most cases the donor resonances show no hf or shf structure and a defect identification can only be based on the g-factors. There are many resonances known, where the defect could not be identified. The broadening effect is less important for 'deep level' defects. One way to overcome this difficulty would be to measure the ODESR spectrum with time resolution. It was shown for shallow In donors in ZnO that the resolution can be greatly enhanced by exciting the luminescence with pulsed light and by taking only the long lifetime tails of the luminescence for the ODESR measurement, which comes from the distant donor-acceptor pairs for which the exchange interaction is only small (46). Little work was done so far with time resolved ODESR in solid state defects.

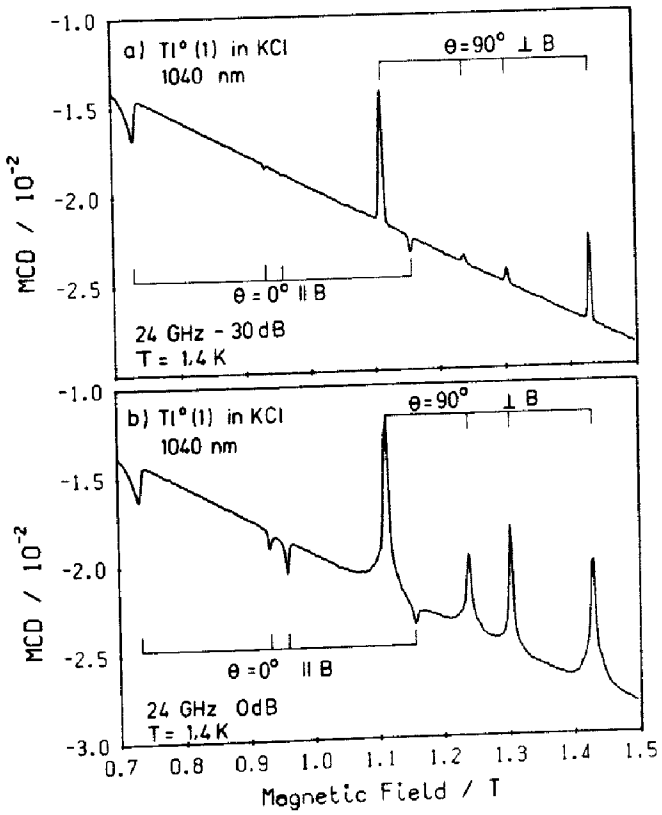

Fig. 30. (a) ODESR spectrum of $Tl^0(1)$ centres in KCl detected as microwave-induced change of the MCD of the absorption band at 1040 nm, measured at low microwave power (24 GHz, T = 1.5 K), (b) the same for high microwave power. After (48).

The investigation of a ground state ESR with optical detection has recently become of particular interest. The reasons are the enhanced sensitivity, its selectivity and the possibility to directly correlate optical bands with ESR spectra and thus with the defect structure. The experiment is based on the observation of the microwave-induced change of the magnetic circular dichroism (MCD) of an absorption band. In Fig.29 it is schematically indicated for an 'atomic' optical transition s → p how the method works.

The allowed optical absorption transition for right and left circular polarised light are indicated along with the relative matrix elements. The absorptions for both polarisations are split in energy by the spin orbit splitting of the excited state. If this splitting is small compared to the phonon width of the absorption bands the measurement of the MCD as a function of photon energy yields a derivative structure.

The MCD is defined as

$$MCD = \frac{d}{4} (\alpha_+ - \alpha_-) \qquad 7.5$$

where d is the crystal thickness, α_+ is the absorption constant for right and α_- for left circular polarised light. If the absorption comes from a Kramers doublet with S = 1/2, one obtains (47)

$$MCD = \frac{1}{2} \alpha_0 \, d \, \frac{\sigma_+ - \sigma_-}{\sigma_+ + \sigma_-} \, \frac{n_- - n_+}{n_- + n_+} \qquad 7.6$$

α_0 is the absorption constant for unpolarised, light σ_+ and σ_- are the cross sections for right and left polarised light, respectively, and n_+ and n_-

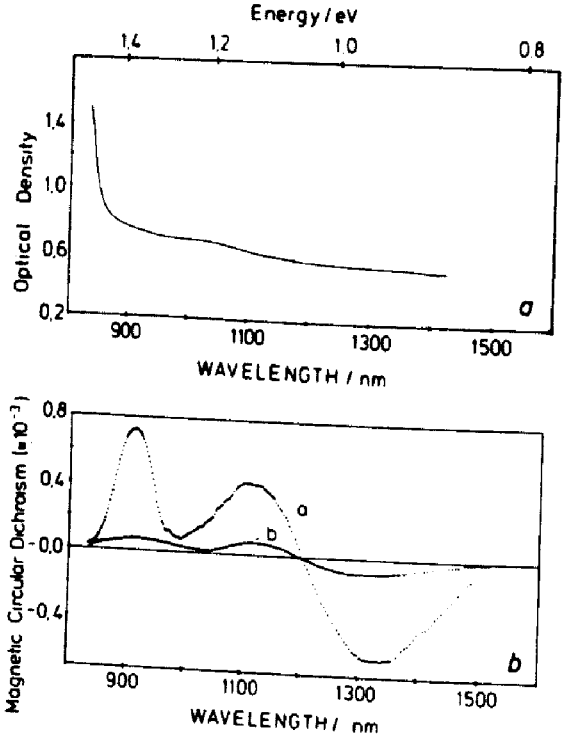

Fig. 31. (a) Optical absorption of LEC-grown undoped 'as-grown' semi-insulating GaAs, (b) magnetic circular dichroism of the absorption (MCD) of the same crystal. (B = 2 T, T = 4.2 K) (Curve a). Curve b is the 'MCD-tagged by ESR'. After (49).

are the occupation numbers for the $m_s = \pm 1/2$ states. The MCD is thus proportional to the occupation difference $n_+ - n_-$ and the cross section difference $\sigma_+ - \sigma_-$.

The occupation difference $n_+ - n_-$ can be decreased by a microwave transition, provided the transition rate is of the order or larger than the spin lattice relaxation rate $1/T_1$. Such an ESR transition thus results in a decrease of the MCD, which is monitored (see Fig. 29). One measures the MCD as a function of the magnetic field under microwave irradiation. The decrease due to the resonance is observed on the variation of the MCD as a function of the magnetic field according to

$$\text{MCD} \propto \tanh\ (g\beta_e B/2kT) \qquad 7.7$$

For low temperatures and the usual field variation this is practically a linear function of B. As an example Fig. 30 shows the ODESR spectrum measured in the absorption band at 1040 nm of the laseractive thallium centres in KCl. (48) (see sections 2 and 3). This absorption has a paramagnetic MCD as expected. It is negative. From Fig. 30 one sees immediately that not a single ESR line appears near g ≈2 as would be expected for an $F_A(Tl^+)$ centre, but altogether 8 transitions. Comparison with the $Tl^0(1)$ centres ESR data (12) shows that the ODESR spectrum can be described exactly by their data (calculated for K-band, 24 GHz). Thus the laser-active centres are indeed identical with the $Tl^0(1)$ centres previously investigated by conventional ESR (48). Here a direct correlation with the optical absorption band at 1040 nm was possible. The ODESR spectrum contains allowed transitions of centres with their axes parallel and perpendicular to the field orientation (indicated in Fig. 30) as well as 'forbidden' transitions, in which also the Tl nuclear quantum numbers change. Their intensity decreases with decreasing microwave power

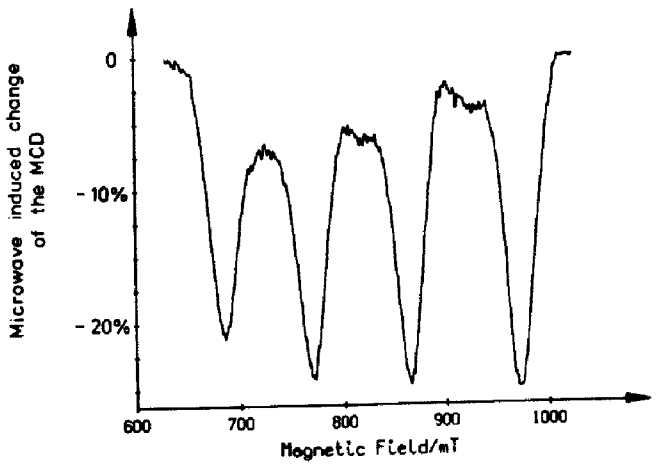

Fig. 32. ODESR spectrum of anion antisite defects $AsAs_4$ in s.i. undoped GaAs 'as-grown'. ($B_o \| [100]$, T = 1.4 K, ν_{ESR}=24 GHz, measured at λ = 1350 nm). After (49).

(see Fig. 30a and 30b). The centre axis is, as mentioned before, the connection line between the $T1^o$ atom and the anion vacancy. (For details see Ref. 48).

Fig. 31 shows the optical absorption and the MCD of 'as-grown' undoped GaAs, which was grown with the LEC (liquid encapsulated Czochralski) method. In the absorption below the gap energy of 1.52 eV only a very weak band at 1.18 eV due to the so called EL2-defects is detectable, whereas the MCD measurement reveals the existence of further intracentre absorption bands due to paramagnetic defects. In the direct measurement the absorption is not detectable. The sensitivity enhancement when measuring the MCD is a consequence of the applied form of modulation spectroscopy (49).

When measuring the ODESR in this MCD, e.g. at 1350 nm, the spectrum of Fig. 32 is observed, which is due to $AsAs_4$ antisite defects, that is due to As atoms on a Ga site analogous to the PP_4 defects in GaP discussed above. The splitting into 4 lines is due to the hf interaction with the central ^{75}As nucleus (I = 3/2). The ESR of antisite defects in as-grown material is very weak, the signal to noise ratio is only of the order of 2-4 (concentration approx. 10^{16} cm^{-3}). Here the signal to noise ratio is better by about 2 orders of magnitude. It should be mentioned, however, that the antisite defects observed in ODESR have a T_1 of several seconds at 1.4 K, while those observed in conventional ESR have a very short T_1 ($\sim 10^{-5}$ sec.) (50). Therefore, both species are different although the spectra look the same and at present it cannot be said, which is the concentration of those measured in ODESR. Possibly, the signal to noise gain is even higher than 2 orders of magnitude. With present techniques the MCD can be measured down to $2\text{-}5 \cdot 10^{-5}$ for an optical density of one.

8. EXCITATION SPECTROSCOPY OF ODESR

The optical detection of ESR spectra opens up the possibility to observe the ESR lines upon variation of the optical wavelength. This can be particularly useful for the determination of all the optical transitions belonging to one particular defect even if these transitions are buried under optical absorption (or emissions) of simultaneously present different defects.

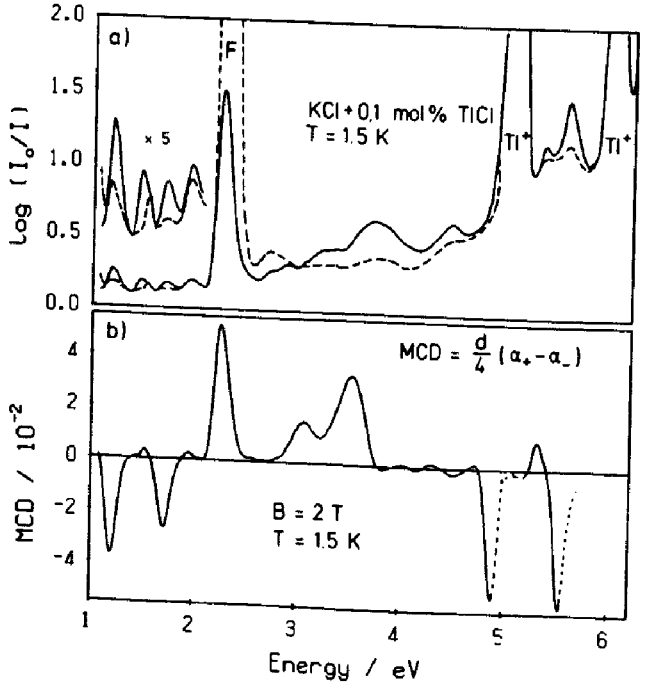

Fig. 33. (a) Absorption spectrum of KCl:Tl after X-irradiation at -40 °C (dashed line) and after F centre bleaching (solid line), (b) magnetic circular dichroism (MCD) of the bleached sample. After (48).

Fig. 33 shows again for the example of the $Tl^0(1)$ centres in KCl the optical absorption spectrum and the MCD spectrum measured after producing the $Tl^0(1)$ centres with X-irradiation at -40 °C, upon which many other defects, many of them Tl-related, are also created. In order to identify the absorption bands belonging to the $Tl^0(1)$ centres, one can monitor the ODESR of one particular ESR line (e.g. of the parallel or perpendicular spectrum for $B_0 \| (100)$), and change the wavelength of the light inducing the optical absorption transitions. Since the level scheme of Fig. 29 does not specify a particular excited state, the ODESR is always observed, if a spin orbit split excited state is reached. Thus, the excitation spectrum of the ODESR lines reveals all those optical absorptions, which belong to one particular centre (or centre orientation). Fig. 34 shows this for parallel and perpendicular $Tl^0(1)$ centres in KCl. Altogether 8 optical $Tl^0(1)$ absorptions could be detected in this way (48,51). This kind of excitation spectrum was called 'MCD-tagged by ESR' (48). A Tl-dimer centre with very similar optical properties as the $Tl^0(1)$ centre but with a completely different ESR spectrum could be separated and analysed with this method too. In the case of the analogous $Ga^0(1)$ and $In^0(1)$ centres the positions of the absorption bands could only be detected in this way, since they were buried in shoulders of other much stronger absorptions (53) and had no emissions, which in principle could also be used to detect other absorption bands by measuring the excitation spectrum of the emission. In the case of the $Tl^0(1)$ centres this was also not possible since the mentioned Tl-dimer centres emitted at the same wavelength as the $Tl^0(1)$ centres.

Another kind of excitation spectroscopy can be performed in semiconductors. The aim is to unambiguously determine the level of a defect in the gap, the structure of which is known from ESR. The usual methods like DLTS (deep level transient spectroscopy) or related methods can determine the energy position of the level, but not identify the corresponding defect. The method is based on a suitable position of the Fermi level such, that the level in question is not occupied. It is then

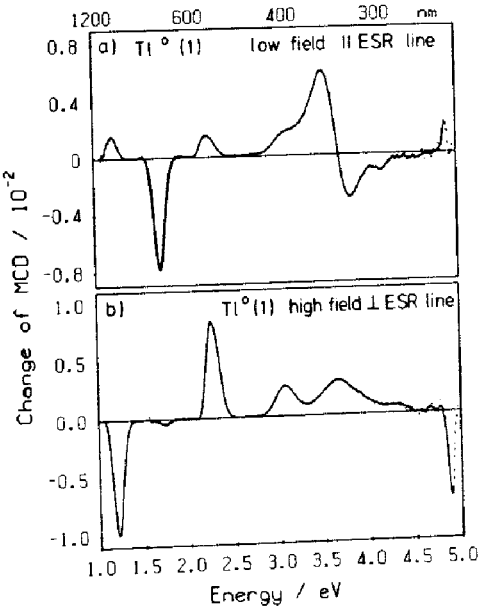

Fig. 34. (a) Magnetic circular dichroism (MCD) at 1.4 K of the 'parallel' $Tl^{o}(1)$ centres in KCl as tagged by the corresponding low field ESR line, (b) the same for 'perpendicular' $Tl^{o}(1)$ centres tagged by the high field ESR line. After (48).

occupied with a second light beam from the valence band, while the first light beam is used to measure the ODESR via, e.g. a microwave-induced decrease of the MCD.

A recent example is the investigation of the antisite defects $AsAs_4$ in p-type GaAs. Before occupying the D^{+}/D^{++} level with electrons from the valence band no MCD can be measured. In Fig. 35 the onset of the MCD is plotted as a function of the wavelength of the exciting light ('second beam'). As from 0.52 eV onwards the MCD can be detected and also the ESR spectrum. From 0.74 eV onwards the MCD decreases again, since the paramagnetic $AsAs_4$ defect captures a second electron and becomes diamagnetic (D^{o}/D^{+} level) (54). The method can be characterised as 'photo ODESR' measurement in analogy to similar experiments performed earlier in conventional ESR (55).

9. OPTICALLY DETECTED ENDOR

As mentioned in the section on ESR for a structure determination of defects it is desirable to resolve the shf structure and thus to measure ENDOR. This is in principle also possible with optical detection and thus to combine its advantages with the higher resolution of shf interactions, which is characteristic for ENDOR. However, only very few experiments of this kind of tripel resonance were reported for solid state defects. One 'self-ENDOR' experiment, that is ENDOR with the central nucleus, was reported on shallow In donors in ZnO, where the tripel resonance was monitored via the donor-acceptor recombination luminescence (46). Another experiment uses the microwave-induced decrease of the MCD and is schematically explained in Fig. 36 for the case of $S = 1/2$, a central nucleus of $I_c = 3/2$ and one ligand nucleus of $I_l = 3/2$, which is the (simplified) scheme for the $AsAs_4$ antisite defects in GaAs. In the experiment one sets the magnetic field onto a particular position in the ODESR line, e.g. into

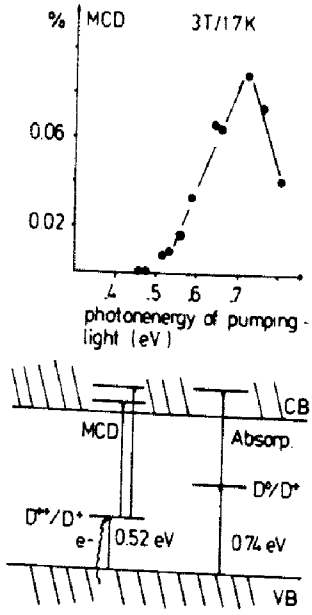

Fig. 35. Excitation spectrum of the ODESR lines of anion antisite $AsAs_4$ defects as measured by photo-ODESR and the resulting level position for the two charge states of the defect.

the flank. The microwave then induces transitions between a particular combination of $m_{I,c}$ and $m_{I,l}$ states. Thus, only the population difference between these states is diminished (equalised in the extreme case). Therefore, only a subset of spin packets contributes to the decrease of the MCD, which is monitored. The microwave is 'sharp' enough not to hit more than this subset of m_I values if spin diffusion etc. is neglected. If then an NMR frequency is simultaneously applied, which combines the $m_{I,l}$ states with its neighbouring ones, then more spin packets are shifted into the microwave pump channel and contribute to the decrease in MCD. Thus, upon such an NMR resonance the decrease of the MCD is enhanced. This is monitored for the detection of this tripel resonance.

Fig. 37 shows the ODENDOR spectrum of $AsAs_4$ defects in semi-insulating 'as-grown' GaAs/Cr. In Fig. 37a the ENDOR lines are due to the nearest ^{75}As neighbours, in Fig. 37b due to the second nearest ^{75}As neighbours (56,57). Their angular dependence could be measured and analysed.

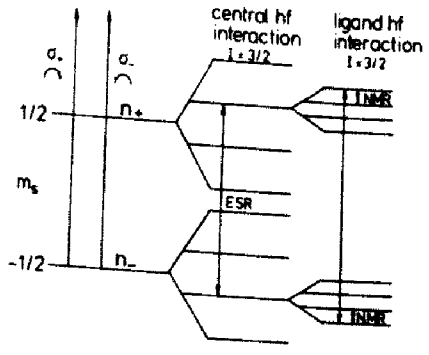

Fig. 36. Level scheme to explain the mechanism of the ODENDOR experiment (see text).

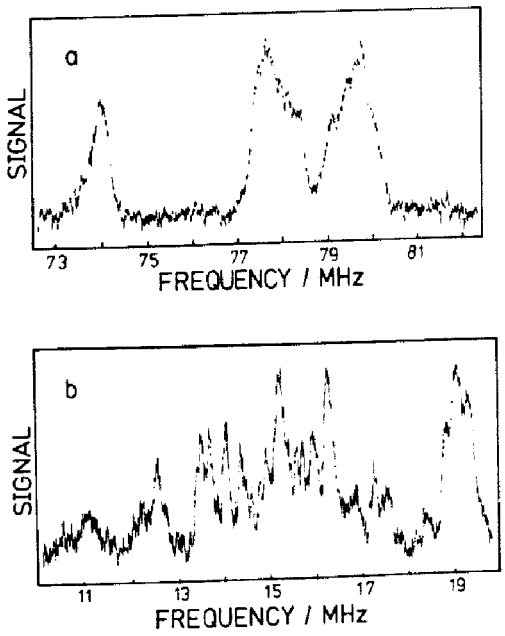

Fig. 37. (a) Part of the ENDOR spectrum of $AsAs_4$ antisite defects in 'as-grown' s.i. GaAs:Cr resolving the shf interaction of nearest ^{75}As neighbours. ($B_0 \| 3^0$ off [110], B_0 = 989 mT, ν_{ESR} = 24.1 GHz, T = 1.6 K, measured at λ = 1320 nm), (b) ENDOR lines due to second nearest ^{75}As neighbours. After (56,57).

It turned out that in GaAs:Cr a regular antisite defect with 4 equivalent next neighbours exists as well as distorted antisite defects in approximately the same concentration (56). Attempts to measure the conventional ENDOR on this sample failed due to the very low signal to noise ratio of the ESR (see also section 8).

Unlike in conventional ENDOR it was found that the ENDOR effect is of the same order as the ESR effect, which is apart from the sensitivity enhancement through the optical detection a great advantage compared to conventional ENDOR, where the effect is usually smaller than 1% of the ESR effect. However, quantitatively, the size of the observed signals is not yet understood. It should also be mentioned, that a technical difficulty is to bring enough rf power into the cavity, which is at 1.4 K pumped helium to saturate the NMR transitions. Low temperature is necessary according to equ. (7.7) to increase the MCD and one works with less noise if the temperature is below the λ point of helium. (The MCD can be very small).

Another advantage of the optically detected ENDOR is that similarly to the 'MCD-tagged by ESR' one can also measure the MCD tagged by 'ENDOR'. This experiment was successfully done in the case of $AsAs_4$ antisite defects and shows that indeed the total MCD of Fig. 29 belongs to the antisite defects and that they have two optical intracenter transitions (see Fig. 33) (49). This possibility is particularly interesting in that it enables to establish a direct correlation between optical bands and details of the defect structure as revealed by the highly resolving ENDOR method.

Conclusion. It was the aim of this article to show that for the structure determination of point defects the use of multiple magnetic resonance methods are very powerful and that the availability of modern experimental techniques makes it possible to tackle also difficult problems

interesting for materials science. The development of these methods is by no means finished. In particular, the optical method can be extended further to time resolved measurements and to experiments, where a spatial resolution of defect distributions can be measured. The increase in sensitivity can be driven further, which is of particular interest for defect studies in thin layers or interfaces.

REFERENCES

1. W.B. Fowler, Ed., Physics of Color Centers, Acad. Press, N.Y. and London (1968)
2. W. Gellermann, K.B. Koch and F. Lüty, Laser Focus (April) 71, 1981
3. G.H. Dieke, Spectra and Energy Levels of Rare-Earth Ions in Crystals, Interscience, New York 1968
4. A.E. Hughes and W.A. Runciman, Proc. Phys. Soc. London, 86, 615 (1965)
5. D.B. Fitchen, Chapter 5 in: "Physics of Color Centers", Ed., W.B. Fowler, Acad. Press, N.Y. and London, 1968
6. A.E. Hughes, "Optical techniques and an introduction to the symmetry properties of point defects' in: "Defects and their Structure in Non-metallic Solids", Eds. B. Henderson and A.E. Hughes, Plenum Press, Nato Advanced Study Inst. Series B, 19 (1976)
7. D.L. Dexter, C.C. Klick and G.A. Russell, Phys. Rev. 100, 603 (1955)
8. R.H. Bartram and A.M. Stoneham, Solid State Comm. 17, 1593 (1975)
9. G.E. Pake and T.L. Estle, The Physical Principles of Electron Paramagnetic Resonance, W.A. Benjamin, Inc., Reading, Mass., 1973
10. C.P. Slichter, Principles of Magnetic Resonance, Harper and Row, N.Y. 1963
11. H.G. Grimmeiss, E. Janzen, H. Ennen, O. Schirmer, J. Schneider, R. Wörner C. Holm, E. Sirtl and P. Wagner, Phys. Rev. B 24, 4571 (1981)
12. E. Goovaerts, J.A. Andriessen, S.V. Nistor and D. Schoemaker, Phys. Rev. B 24, 29 (1981)
13. J.-M. Spaeth, "Atomic hydrogen as a model defect in alkali halides" in: "Defects in Insulating Crystals", Eds. V.M. Tuchkevich and K.K. Shvarts, Springer, Berlin, Heidelberg, New York 1981, p. 232
14. G. Feher, Phys. Rev. 114, 1219, 1249 (1959)
15. H. Seidel, Z. Physik 165, 218, 239 (1961)
16. G. Heder, J.R. Niklas and J.-M. Spaeth, phys. stat. sol. (b) 100, 567 (1980)
17. Y. Ueda, J.R. Niklas, J.-M. Spaeth, R. Kaufmann and J. Schneider, Solid State Comm. 46, 127 (1983)
18. S. Greulich-Weber, J.R. Niklas, E. Weber and J.-M. Spaeth, Phys. Rev. B 30, 6292 (1984)
19. J.R. Niklas, Habilitationsschrift, Paderborn 1983
20. M.U.A. Bromba and Horst Ziegler, Analytical Chemistry 51, 1760 (1979)
21. H. Ziegler, Applied Spectroscopy 35, 88 (1981)
22. M.U.A. Bromba and H. Ziegler, Analytical Chemistry 55, 648 (1983)
23. U.U.A. Bromba and H. Ziegler, Analytical Chemistry 56, 2052 (1984)
24. Y. Ueda, J.R. Niklas and J.-M. Spaeth, Solid State Comm. 46, 121 (1983)
25. S. Greulich-Weber, J.R. Niklas and J.-M. Spaeth, J. Phys. C: Solid State Phys. 17, L911 (1984)
26. H. Söthe, P. Studzinski and J.-M. Spaeth, phys. stat. sol. (b) 130, 339 (1985)
27. H. Söthe, P. Studzinski and J.-M. Spaeth, to be published
28. Ch. Hoentzsch and J.-M. Spaeth, phys. stat. sol. (b) 94, 479 (1979)
29. P. Studzinski, J.R. Niklas and J.-M. Spaeth, phys. stat. sol. (b) 101, 673 (1980)
30. P. Studzinski and J.-M. Spaeth, Radiation Effects 73, 207 (1983)
31. P. Studzinski, Dissertation, Paderborn 1985
32. J.R. Niklas and J.-M. Spaeth, phys. stat. sol. (b) 101, 221 (1980)
33. J.-M. Spaeth and J.R. Niklas, Condensed Mater Physics 1, 393 (1981)

34. R.C. DuVarney, J.R. Niklas and J.-M. Spaeth, phys. stat. sol. (b) 97, 135 (1980)
35. R. Biehl, M. Plato and K. Möbius, J. Chem. Phys. 63, 3515 (1975)
36. N.S. Dalal and C.A. McDowell, Chem. Phys. Letts. 6, 617 (1970)
37. J.R. Niklas, R.U. Bauer and J.-M. Spaeth, phys. stat. sol. (b) 119, 171 (1983)
38. R.C. DuVarney, J.R. Niklas and J.-M. Spaeth, phys. stat. sol. (b) 128, 673 (1985)
39. P. Edel, C. Hennies, Y. Merle d'Aubigné, R. Romestain and Y. Twarowsky, Phys. Rev. Letts. 28, 1268 (1972)
40. P. Dawson, C.M. McDonagh, B. Henderson and L.S. Welch, J. Phys. C: Solid State Phys. 11, L983 (1978)
41. F.J. Ahlers, F. Lohse and J.-M. Spaeth, Solid State Comm. 43, 321 (1982)
42. J.D. Dunstan and J.J. Davies, J. Phys. C: Solid State Phys. 12, 2927 (1979)
43. K.P. O'Donnell, M.K. Lee and G.D. Watkins, Solid State Comm. 44, 1015 (1982)
44. N. Killoran, B.C. Cavenett, M. Godlewski, A.T. Kennedy and N.D. Wilsey, Physica B 116, 425 (1982)
45. B.K. Meyer, Th. Hangleiter, J.-M. Spaeth, G. Strauch, Th. Zell, A. Winnacker and R.H. Bartram, J. Phys. C: Solid State Phys. 18, 1503 (1985)
46. D. Block, A. Hervé and R.T. Cox, Phys. Rev. B 25, 6049 (1982)
47. L.F. Mollenauer and S. Pan, Phys. Rev. B 6, 772 (1972)
48. F.J. Ahlers, F. Lohse, J.-M. Spaeth and L.F. Mollenauer, Phys. Rev. B 28, 1249 (1983)
49. B.K. Meyer, J.-M. Spaeth and M. Scheffler, Phys. Rev. Letts. 52, 851 (1984)
50. J.-M. Spaeth and B.K. Meyer, Festkörperprobleme XXV, 614 (1985)
51. F.J. Ahlers, Dissertation, Paderborn 1985
52. F.J. Ahlers, F. Lohse and J.-M. Spaeth, J. Phys. C: Solid State Phys. 18, 3881 (1985)
53. F.J. Ahlers, F. Lohse, Th. Hangleiter, J.-M. Spaeth, R.H. Bartram, J. Phys. C: Solid State Phys. 17, 4877 (1984)
54. B.K. Meyer, D. Hofmann and J.-M. Spaeth, to be published
55. U. Kaufmann and J. Schneider, Festkörperprobleme XX, 87 (1980)
56. D.M. Hofmann, B.K. Meyer, F. Lohse and J.-M. Spaeth, Phys. Rev. Letts. 53, 1187 (1984)
57. J.-M. Spaeth, D.M. Hofmann and B.K. Meyer, Proc. of the Mat. Research Society Conf. in San Francisco 1985.